# REPORT DOCUMENTATION PAGE

*Form Approved*
*OMB No. 0704-0188*

The public reporting burden for this collection of information is estimated to average 1 hour per response, including the time for reviewing instructions, searching existing data sources, gathering and maintaining the data needed, and completing and reviewing the collection of information. Send comments regarding this burden estimate or any other aspect of this collection of information, including suggestions for reducing the burden, to Department of Defense, Washington Headquarters Services, Directorate for Information Operations and Reports (0704-0188), 1215 Jefferson Davis Highway, Suite 1204, Arlington, VA 22202-4302. Respondents should be aware that notwithstanding any other provision of law, no person shall be subject to any penalty for failing to comply with a collection of information if it does not display a currently valid OMB control number. **PLEASE DO NOT RETURN YOUR FORM TO THE ABOVE ADDRESS.**

| 1. REPORT DATE *(DD-MM-YYYY)* | 2. REPORT TYPE | 3. DATES COVERED *(From - To)* |
|---|---|---|
| 12/01/2015 | Final Technical report | 01 Feb 2012-30 Sep 2015 |

**4. TITLE AND SUBTITLE**
Hydroacoustics of Beveled Steps and Gaps

**5a. CONTRACT NUMBER**

**5b. GRANT NUMBER**
N00014-12-1-0373

**5c. PROGRAM ELEMENT NUMBER**

**6. AUTHOR(S)**
Glegg, Stewart A.L.

**5d. PROJECT NUMBER**

**5e. TASK NUMBER**

**5f. WORK UNIT NUMBER**

**7. PERFORMING ORGANIZATION NAME(S) AND ADDRESS(ES)**
Florida Atlantic University, 777 Glades Road, Boca Raton, FL 33431

**8. PERFORMING ORGANIZATION REPORT NUMBER**

**9. SPONSORING/MONITORING AGENCY NAME(S) AND ADDRESS(ES)**
Office of Naval Research
875 Randolph Street
Arlington, VA 22203-1995

**10. SPONSOR/MONITOR'S ACRONYM(S)**

**11. SPONSOR/MONITOR'S REPORT NUMBER(S)**

**12. DISTRIBUTION/AVAILABILITY STATEMENT**
Approved for public release

**13. SUPPLEMENTARY NOTES**

**14. ABSTRACT**
This report describes the work carried out under grant number N00014-12-1-0373 "Hydroacoustics of Beveled Steps and Gaps" at Florida Atlantic University. The project was in collaboration with Dr. William Devenport of Virginia Tech, who has carried out wind tunnel measurements on the steps and obstructions described in this report as part of a companion project. The overall objective of this study is to measure and predict the sound radiation from steps and gaps on large pales excited by turbulent boundary layers. Results are given showing the methods used to calculate the far field noise levels and how this is related to the boundary layer turbulence associated with different types of step.

**15. SUBJECT TERMS**
Aeroacoustics, hydroacoustics, turbulent flow, steps

| 16. SECURITY CLASSIFICATION OF: | | | 17. LIMITATION OF ABSTRACT | 18. NUMBER OF PAGES | 19a. NAME OF RESPONSIBLE PERSON |
|---|---|---|---|---|---|
| a. REPORT | b. ABSTRACT | c. THIS PAGE | | | Glegg, Stewart A. L. |
| U | U | U | SAR | 62 | 19b. TELEPHONE NUMBER *(Include area code)* 561 297 2633 |

**Standard Form 298** (Rev. 8 '98)
Prescribed by ANSI Std. Z39.18

20151221035

# INSTRUCTIONS FOR COMPLETING SF 298

**1. REPORT DATE.** Full publication date, including day, month, if available. Must cite at least the year and be Year 2000 compliant, e.g. 30-06-1998; xx-06-1998; xx-xx-1998.

**2. REPORT TYPE.** State the type of report, such as final, technical, interim, memorandum, master's thesis, progress, quarterly, research, special, group study, etc.

**3. DATE COVERED.** Indicate the time during which the work was performed and the report was written, e.g., Jun 1997 - Jun 1998; 1-10 Jun 1996; May - Nov 1998; Nov 1998.

**4. TITLE.** Enter title and subtitle with volume number and part number, if applicable. On classified documents, enter the title classification in parentheses.

**5a. CONTRACT NUMBER.** Enter all contract numbers as they appear in the report, e.g. F33315-86-C-5169.

**5b. GRANT NUMBER.** Enter all grant numbers as they appear in the report. e.g. AFOSR-82-1234.

**5c. PROGRAM ELEMENT NUMBER.** Enter all program element numbers as they appear in the report, e.g. 61101A.

**5e. TASK NUMBER.** Enter all task numbers as they appear in the report, e.g. 05; RF0330201; T4112.

**5f. WORK UNIT NUMBER.** Enter all work unit numbers as they appear in the report, e.g. 001; AFAPL30480105.

**6. AUTHOR(S).** Enter name(s) of person(s) responsible for writing the report, performing the research, or credited with the content of the report. The form of entry is the last name, first name, middle initial, and additional qualifiers separated by commas, e.g. Smith, Richard, J, Jr.

**7. PERFORMING ORGANIZATION NAME(S) AND ADDRESS(ES).** Self-explanatory.

**8. PERFORMING ORGANIZATION REPORT NUMBER.** Enter all unique alphanumeric report numbers assigned by the performing organization, e.g. BRL-1234; AFWL-TR-85-4017-Vol-21-PT-2.

**9. SPONSORING/MONITORING AGENCY NAME(S) AND ADDRESS(ES).** Enter the name and address of the organization(s) financially responsible for and monitoring the work.

**10. SPONSOR/MONITOR'S ACRONYM(S).** Enter, if available, e.g. BRL, ARDEC, NADC.

**11. SPONSOR/MONITOR'S REPORT NUMBER(S).** Enter report number as assigned by the sponsoring/ monitoring agency, if available, e.g. BRL-TR-829; -215.

**12. DISTRIBUTION/AVAILABILITY STATEMENT.** Use agency-mandated availability statements to indicate the public availability or distribution limitations of the report. If additional limitations/ restrictions or special markings are indicated, follow agency authorization procedures, e.g. RD/FRD, PROPIN, ITAR, etc. Include copyright information.

**13. SUPPLEMENTARY NOTES.** Enter information not included elsewhere such as: prepared in cooperation with; translation of; report supersedes; old edition number, etc.

**14. ABSTRACT.** A brief (approximately 200 words) factual summary of the most significant information.

**15. SUBJECT TERMS.** Key words or phrases identifying major concepts in the report.

**16. SECURITY CLASSIFICATION.** Enter security classification in accordance with security classification regulations, e.g. U, C, S, etc. If this form contains classified information, stamp classification level on the top and bottom of this page.

**17. LIMITATION OF ABSTRACT.** This block must be completed to assign a distribution limitation to the abstract. Enter UU (Unclassified Unlimited) or SAR (Same as Report). An entry in this block is necessary if the abstract is to be limited.

# The Hydroacoustics of Beveled Steps and Gaps
## Final Technical Report to the Office of Naval Research
### (Technical Monitor: Ronald Joslin)

Stewart Glegg and Benjamin S. Bryan
November 2015

In the last few years there have been some enlightening experimental and numerical studies on the sound radiated by turbulent flow over steps and gaps. These studies are particularly important for the design of quiet marine vehicles where the tolerances of plate joints need to be specified, and on aircraft fuselages where interior noise is an issue. However none of these studies have provided the appropriate scaling of the source terms that can be used to predict the sound radiated from steps and gaps at full scale. The purpose of this study was to develop these scaling laws by combining the results of a detailed experimental study at Virginia Tech (VT) with the appropriate analytical models.

The work has been carried out in collaboration with Dr. William Devenport at Virginia Tech who carried out experimental studies on the steps and obstructions described in this report, and Dr. Meng Wang from the University of Notre Dame who carried out companion numerical studies. The work is summarized in the PhD Dissertation of Benjamin Bryan who successfully defended his work in September 2015. Two papers describing the details of this study are attached to this report and the major findings are summarized below.

*Technical Achievements:*

In the first year of this study the sound radiation from a boundary layer flow over a forward facing step was characterized in terms of surface pressure fluctuations. Previous theories modeled this source as a streamwise dipole whose strength is determined by the pressure fluctuations on the face of the step. The pressure fluctuations on the top surface of the step were considered to be of quadrupole order and therefore neglected. However wind tunnel measurements at Virginia Tech showed that the surface pressure fluctuations in the separation zone just downstream of the step were approximately 30dB higher than those just forward of the step and it was shown theoretically that these higher levels can overcome the quadrupole/dipole scaling differential so the separation zone is the primary source of the radiated sound.

In the second year of the study the sound radiation from beveled steps and the details of the unsteady loadings on the different surfaces of the step were investigated. On the basis of measurements by Cattlett (2010) it was assumed that self noise sources caused by separated flow at the corner dominate the far field sound radiation. A formula was derived for the unsteady loading on a corner, which showed that the net unsteady force on the surface is directed from the corner to a point in the separation bubble, that it scales inversely with the distance of the vorticity from the corner, and the square of the vorticity amplitude. The predicted directivity plots of the far field sound compared well with measurements and the scaling of the far field/surface pressure spectra for beveled steps is consistent with the model.

It was also found that a two dimensional model of the flow was able to scale the far downstream surface pressure spectra on a self similar function and to extract the scaling of the spectra with distance downstream which is consistent with measurements (Awasthi *et al.* (2011)). The flow was modeled by a separation bubble that periodically sheds vorticity or coherent structures. The characteristics of the

unsteady surface pressure were well predicted and found to be proportional to the square of the circulation in the shed vorticity. The linear interaction of the mean flow with the shed vorticity has a second order effect on the surface pressure and this interaction can be ignored at large distances downstream from the separation bubble. The calculated surface pressure spectrum was compared to measurements and excellent agreement was found by matching three modeling parameters to the data: the convection velocity, the mean height of the shed vorticity above the surface, and a coefficient that describes the probability function of the height of the shed vortex above the surface.

In the third year of the study it was shown that, regardless of the details of the flow, the unsteady loading on each surface of the corner is the same and this controls the directionality of the far field sound. Comparisons are made with measured far field sound spectra with excellent agreement. The role of the shed vorticity on the unsteady loading was also investigated and it is concluded that it has a second order effect. The primary source of the unsteady loading on the corner is determined by the unsteady growth and motion of the separation bubble, which will depend on its interaction with the corner and the application of the Kutta condition.

During the past year we have considered the flow around a three dimensional cylindrical embossment of very low aspect ratio mounted on a plate. The sound radiation from this flow has been predicted using the theory developed in previous years, along with RANS simulation that describes the mean flow. Details are given in the PhD Dissertation of B. Bryan, listed below. Both flow and noise predictions were compared with wind tunnel measurements taken at Virginia Tech. Both the simulations and the wind tunnel measurements showed that the cylinder exhibits a separation zone on the leading half of the cylinder, which is similar to the separation zone on a forward facing step. With this similarity, and the application of the sweep independence principle, a prediction method for the sound radiation from flow over a cylindrical embossment was developed. The approach was to separate the edge of the cylinder into elements, which behave as forward-facing steps with an angle of incidence relative to the flow. The sum of the sources over the surface of the cylinder then gave the total sound field. The application of an empirical fit to the sound spectra for flow over a forward-facing step, with one modified parameter, gives the spectral shape and scaling of the sound from the cylinder. Comparison with measurements made at Virginia Tech in the companion study showed that there is a close agreement between the measured and predicted spectra.

More details regarding these results can be found in the two attached papers. Additional papers are in preparation for publication in the AIAA Journal

Publications
    Publications appearing during the period of performance are listed citing the support of this project or its predecessor (N00014-08-1-1122)

Glegg, S. A., B. Bryan, W. J. Devenport and M. Awasthi (2014). The Noise From Separated Flow. 20th AIAA/CEAS Aeroacoustics Conference. Atlanta GA. AIAA paper number 2014-2460

Bryan, B. S., S. Glegg, M. Awasthi and W. Devenport (2015). Noise Radiation from a Cylindrical Embossment Immersed in Turbulent Boundary Layer Flow. Aviation 2015. Dallas, TX. AIAA paper number 2015-3270

Bryan, B.S. (2012). "Noise Radiation From Small Steps And Cubic Roughness Elements Immersed In Turbulent Boundary Layer Flow", MS, Florida Atlantic University.

Bryan, B.S. (2015). "Noise Radiation From a Cylindrical Embossment Immersed In Turbulent Boundary Layer Flow", PhD, Florida Atlantic University.

S.A.L. Glegg, "The Tailored Greens Function for a Forward Facing Step" *Journal of Sound and Vibration*, 332(2013) pp 4037-4044

Glegg, S., M. Bryan, W. J. Devenport and M. Awasthi (2012). Sound Radiation from Forward Facing Steps. 18th AIAA/CEAS Aeroacoustics Conference. Colorado Springs, Colorado.

B.Bryan and S.Glegg, "The response of a surface discontinuity to an incoming vortex", presented at the 19th AIAA Aeroacoustics Conference, Berlin, Germany, May 26-29, 2013, AIAA paper number 2013-2250

Awasthi, M., B. Bryan, W. Devenport and S. Glegg (2013). Sound Radiation from Rounded Steps and Gaps. 19th AIAA/CEAS Aeroacoustics Conference. Berlin.

Awasthi, M., W. J. Devenport, T. W. Meyers, W. N. Alexander and S. A. Glegg (2014). Aeroacoustics of 2D and 3D Surface Discontinuities. 20th AIAA/CEAS Aeroacoustics Conference. Atlanta, GA.

Awasthi, M., William J. Devenport, Stewart A. L. Glegg and Jonathan B. Forest (2014). "Pressure fluctuations produced by forward steps immersed in a turbulent boundary layer." Journal of Fluid Mechanics **756**: 384-421.

Catlett, M., W. J. Devenport and S. Glegg (2014). "Sound from boundary layer flow over steps and gaps." Journal of Sound and Vibration **333**: 4170-4186.

## Attachments

The detailed technical information described above are attached below. These reports are copies of the papers presented at recent AIAA AVIATION Conferences:

Glegg, S. A., B. Bryan, W. J. Devenport and M. Awasthi (2014). The Noise From Separated Flow. 20th AIAA/CEAS Aeroacoustics Conference. Atlanta GA. AIAA paper number 2014-2460

Bryan, B. S., S. Glegg, M. Awasthi and W. Devenport (2015). Noise Radiation from a Cylindrical Embossment Immersed in Turbulent Boundary Layer Flow. Aviation 2015. Dallas, TX. AIAA paper number 2015-3270

# The Noise from Separated Flows

Stewart Glegg[1] and Benjamin Bryan.[2]
*Florida Atlantic University, Boca Raton, FL 33431*

William Devenport[3] and Manuj Awasthi[4]
*Virginia Tech, Blacksburg, VA*

**This paper will consider a simple two dimensional model of the separated flow downstream of a corner and model the pressure fluctuations on the surface, the unsteady loadings, and the sound radiation. The flow is modeled by a separation bubble that periodically sheds vorticity. The characteristics of unsteady surface pressure are well predicted and found to be proportional to the square of the circulation in the shed vorticity. The linear interaction of the mean flow with the shed vorticity has a second order effect on the surface pressure and this interaction can be ignored at large distances downstream from the separation bubble. The calculated surface pressure spectrum was compared to measurements and excellent agreement was found by matching three modeling parameters to the data: the convection velocity, the mean height of the shed vorticity above the surface, and a coefficient that describes the probability function of the height of the shed vortex above the surface. It is also shown that, regardless of the details of the flow, the unsteady loading on each surface of the corner is the same and this controls the directionality of the far field sound. Comparisons are made with measured far field sound spectra with excellent agreement. The role of the shed vorticity on the unsteady loading is also investigated and it is concluded that it has a second order effect. The primary source of the unsteady loading is determined by the unsteady growth and motion of the separation bubble which will depend on its interaction with the corner and the application of the Kutta condition.**

## I. Introduction

The noise from separated flow is one of the least well understood problems in aero and hydroacoustics. In this paper we will discuss the specific scaling mechanisms for an impulsively started flow over a sharp corner and show how models for the sound radiation from vortex shedding at the edge may be reduced to a simple dipole scaling law that is non-linearly dependent on the strength of the shed vorticity. Although the results have more general applicability to flows that separate at an edge this study will focus on the sound radiation from a corner and a forward facing step. An analytical model will be developed for the surface pressure fluctuations on the step surfaces, and for the dipole source strengths. In particular we will consider the self noise generated by the step, and it will be argued that the measurements by Catlett *et al* (2014) show that this is the dominant source of sound. It will then be shown that vorticity in the vicinity of the upper corner of the step is the dominant source, and that the far field sound is given by a dipole source that is equivalent to a point force located at the top corner of the step and pointing into the separation bubble.

---

[1] Professor, Dept. of Ocean and Mechanical Engineering, and AIAA Associate Fellow.
[2] Graduate Student, Dept. of Ocean and Mechanical Engineering, and AIAA Student Member.
[3] Professor, Department Aerospace and Ocean Engineering, and AIAA Associate Fellow.
[4] Graduate Student, Department Aerospace and Ocean Engineering and AIAA Student Member

## II. Sound Radiation from Flow over Surface Discontinuities

### A. Background Theory

The sound radiation from flow over stationary rigid surfaces is a direct application of Curle's theorem and is given by

(1)

$$\rho'(\mathbf{x},t)c_\infty^2 = \int\limits_{-T}^{T} \int\limits_{S} p_{ij}(\mathbf{y},\tau)n_j \frac{\partial}{\partial y_i}G(\mathbf{x},t\,|\,\mathbf{y},\tau)dS(\mathbf{y})d\tau + \int\limits_{-T}^{T} \int\limits_{V} T_{ij}(\mathbf{y},\tau)\frac{\partial^2}{\partial y_i \partial y_j}G(\mathbf{x},t\,|\,\mathbf{y},\tau)dV(\mathbf{y})d\tau$$

Where $\rho'$ is the density perturbation, $c_o$ is the speed of sound, $p_{ij}$ is the compressive stress tensor that includes both unsteady pressure and shear stresses applied to the surface, $G$ is a suitable Green's function which is a solution to the wave equation, and $T_{ij}$ is Lighthill's stress tensor. It should be noted that the pressure fluctuations on the surface originate from the turbulent velocity fluctuations in the flow. The origin of all the radiated sound is therefore the turbulent stresses that contribute to $T_{ij}$. However the surface pressure fluctuations play an important role in altering the radiation efficiency of the turbulence and greatly enhancing the far field sound. The surface shear stress is an additional origin of sound, but for high Reynolds number flows these are usually negligible and will be ignored in this analysis.

There is some flexibility in choosing the Green's function in Curle's equation. If a tailored Green's function is chosen whose spatial derivative normal to the surface is zero, then the surface integral is eliminated from equation (1). This is useful because it provides some understanding of the radiation efficiencies for different parts of the flow. However the behavior of the tailored Green's function near corners or sharp edges can be singular. This is also the location where the flow is most difficult to compute or model since viscous effects, the Kutta condition, and vortex shedding prevail at these locations. The alternative is to use the free field Green's function or a Green's function that has a zero normal derivative on one of the surfaces. The surface integral in equation (1) must then be included and this gives terms that are of dipole order, which are far more efficient than the volume sources which are of quadrupole order. Furthermore the pressure fluctuations near the corners will tend to zero because of the Kutta condition and the sensitivity of the far field sound to the local flow at a corner or an edge is greatly reduced if not eliminated. However the turbulent velocity fluctuations in the flow cause acoustic waves that cause pressure fluctuations on the surface, and these can be scattered by surface discontinuities, as well as impacting the velocity fluctuations in the turbulence. The subtleties of these interactions are not well understood, and can only be determined from a comparison of an incompressible flow calculation (Ji and Wang (2010)) with a compressible flow calculation (Slomski (2011)). However even from these detailed numerical studies it is difficult to specify the roles of different source mechanism. An alternative is to model the turbulence by the interaction two dimensional line vortices (Howe (2003)). While this is a very simplistic model of turbulence it contains sufficient physics to identify both the linear and non linear interactions within the turbulent flow, and it provides some insight into the mechanisms that are hidden in a full realization of the flow field. Howe's modeling approach therefore has some advantages when trying to identify the source mechanisms associated with flow over rigid surfaces and will be the approach used here.

### B. Turbulent Flows over Forward Facing Steps

The turbulent flow over a forward facing step is a canonical example of a separated flow. Understanding the mechanisms involved and their relationship to radiated sound is therefore a fundamental problem in aero and hydroacoustics. There has been surprisingly little analytical work in this area in spite of its importance, and so the study of this canonical problem has implications to the sound radiation from separated flow over lifting surfaces or bluff bodies such as aircraft landing gear.

If we consider the unsteady flow over a forward facing step we can identify three origins of turbulence.

1) Upstream turbulence that originates in the turbulent boundary layer or some other surface discontinuity that impinges on the step and causes local pressure fluctuations that are linearly related to the amplitude of incident gusts.

2) Upstream turbulence that causes a non-linear interaction with the separated flow behind the step.

3) Turbulence that originates at the step and causes a separation bubble on the surface downstream of the step.

Howe (2003) discusses the interaction mechanisms 1) and 2) and concluded that if the turbulence in the incoming flow followed a streamline then the force on the forward face of the step was zero. In reality the mean flow separates and the deviation of the turbulent flow from its ideal path will cause unsteady pressure fluctuations on the step face. However the experimental results of Catlett *et al* (2014) suggest that this mechanism is not responsible for the sound radiation. In his experiment Catlett *et al* (2014) measured the sound radiation from a backward facing step in front of a forward facing step. He showed that when the backward facing step was higher than the forward facing step then the sound levels were independent of the forward facing step height. However when the backward facing step was higher than the backward facing step then the sound radiation was independent of the height of the backward facing step and the same as the sound level from the forward facing step without any upstream discontinuity present. This essentially eliminates the interaction mechanisms specified as items 1) and 2), and suggests that the modeling of the flow should be based on turbulence that originates at the step. The immediate implication is that the flow in the separation bubble is the most important region to understand and to model analytically if the sound radiation is to be predicted.

### C. Modeling the Separation Bubble

The separated flow at a corner or and edge (as shown in Figure 1) has been studied using contour dynamics (Pullin (1978), Saffman (1992)), or vortex element methods (Kiya and Saski (1983)). The focus of these studies is the roll up of a spiral vortex that is shed from the corner of the surface discontinuity (Figure 2). The time dependent analysis given by Pullin (1978) and Saffman (1992) is most revealing and shows, by using non dimensional analysis, the time and length scales of the circulation in the separation bubble. The vortex sheet that is shed from an impulsively started flow rapidly rolls up into a tightly wound vortex spiral. After a critical time the experimental studies (Cherry (1984)) show that the vortex spiral bursts and sheds a discrete vortex that is convected downstream. To maintain a steady state, the rate of circulation created at the edge must match the rate of vorticity lost downstream. The non-dimensional scaling therefore gives the magnitude of the circulation in the shed vortex if the timescale of the shedding is known. Measurements (Cherry (1984), Devenport (1991)) suggest that the Strouhal number of vortex shedding from a 90 deg corner is of order 0.1, and so in principle we can estimate the amplitude of the unsteady circulation. However it is not clear that this time scale will also apply to beveled steps, and measurements are needed to ascertain the appropriate time scale.

To calculate the surface pressure from the spiral vortex shedding model described above it is necessary to account for the effect of the surface, and the image vorticity. It is relatively straight forward to use a conformal transformation to map the flow onto a half plane, so the image vorticity is defined analytically. The surface flow speed can also be calculated in the physical domain to give the distribution of time varying surface pressure. This procedure will be laid out in detail below, and shows how the surface pressure will depend on the amplitude of the time varying circulation and the position of the shed vortex as a function of time.

## III.  Self Similar Time Varying Flows over a Corner

First we will consider an analytical model for the pressure fluctuations on the surfaces around the corner by considering a two dimensional model in which the separation bubble is defined by a vortex sheet and a distribution of isolated vortices. The flow separates at the top corner of the step and creates a vortex sheet that breaks down into isolated patches of vorticity that are convected downstream by the mean flow. The surface pressure can be calculated by finding a solution based on potential flow modeling and conformal mapping providing that the distribution of vorticity and its time variation is known. The details of this procedure are straightforward and are given in Howe (2003). The more critical part of the problem is correctly modeling the vorticity in the separation bubble and the downstream flow.

The evolution of a time varying vortex spiral caused by an impulsively started flow at a corner is discussed by Saffman (1996), based on the approach taken by Pullin (1978). They considered the flow

around a sharp edge as shown in Figure 1 with an external angle $\alpha$. In the absence of flow separation the flow can be described by the complex potential

(2)

$$W = At^v Z^\mu$$

where $t$ is time and $v$ is a positive exponent. For an impulsively started flow $v=0$. The physical coordinates are given by $X, Y$ and $Z=X+iY$. The exponent $\mu$ is defined by the wedge angle where

(3)

$$\mu = \frac{\pi}{\pi + \alpha}$$

It follows that $\mathrm{Im}(W)=0$ on the surfaces and for all sharp edges $\frac{1}{2}<\mu<1$. The constant $A$ has dimensions $L^{2-\mu}T^{-1-v}$.

To account for the shed vorticity and its reflection by the surface a correction is added to the complex potential which, from dimensional analysis, must be of the form

(4)

$$W_v = A^{2k}t^n f(Z / A^k t^m) \qquad k = 1/(2-\mu) \qquad m = (1+v)k \qquad n = (2v+\mu)k$$

and we note that $n=2m-1$.

Pullin (1978) shows that the total circulation shed from the corner after a period of time $t$ is given by

(5)

$$\Gamma_s(t) = \left(\frac{1-\mu}{m}\right)^k JA^{2k}t^n$$

where the constant $J$ is part of the self similar solution. For impulsively started flows Pullin gives $J\sim2.4$-$2.5$ for corner angles $\alpha<\pi/2$.

The experimental results of Cherry (1984) suggest that after a critical time period the vortex spiral breaks down and vorticity is shed into the wake. The vortex spiral is therefore re-started or at least returned to its state at time $t_1$ defined by the amount of vorticity shed in a given breakdown. If the shed vorticity is $\Delta\Gamma$ then

(6)

$$\Delta\Gamma = \left(\frac{1-\mu}{m}\right)^k JA^{2k}(t_c^n - t_1^n)$$

gives a non linear relationship between the timescales of the shedding and the amount of vorticity that is shed in a breakdown. Experimental measurements (Cherry (1984)) suggest that the timescale $\Delta t=t_c-t_1$ is given by a Strouhal number of about one based on the reattachment length of the separation bubble.

This model suggests that the unsteady flow is equivalent to a vortex with circulation $\Delta\Gamma$ growing from zero strength to its maximum strength over a time period $\Delta t$ at a fixed point and then being shed and convected downstream by the mean flow without any further change in strength. Figure 2 shows an illustration of this model in which the attached vortex sheet has a net circulation that varies periodically in time and the shed vorticity is represented by isolated regions of vorticity with strength $\Delta\Gamma$.

# IV. The Shed Vorticity

The flow in the separation bubble is difficult to model, but we can draw some insight about the shed vorticity from relatively simple models of the flow. We assume a steady state flow with random perturbations to the separation bubble caused by either upstream disturbances or instabilities in the flow that results in vorticity being intermittently shed from the separation bubble as illustrated in Figure 2. We will assume the circulation in the separation bubble is constant, and treat small perturbations in both strength and position of the bubble as second order effects.

The numerical results of Pullin (1978) and RANS calculations of flow over a step suggest that the mean flow around the separation bubble can be crudely modeled by a vortex located near the surface just downstream of the corner of the step. To consider this we will define a conformal mapping from the physical plane defined by the complex variable $Z$ to upper half plane defined by the variable $z$. For a two dimensional ideal flow around a corner with an external angle $\alpha + \pi$, as defined in Figure 1, the mapping is given by

$$(7)$$

$$\frac{z}{s} = \left(\frac{Z}{L}\right)^{\mu}$$

The ideal potential flow has a singularity at the corner which can be eliminated by placing a vortex in the flow at a location $z_o = x_o + iy_o$ to represent the separation bubble and an image vortex at $z_o{}^*$. The velocity in the physical plane is then defined as

$$(8)$$

$$W_o'(Z) = w_o'(z)\frac{dz}{dZ} = \left(u_e - \frac{i\Gamma_o}{2\pi}\left(\frac{1}{z-z_o} - \frac{1}{z-z_o^*}\right)\right)\frac{dz}{dZ} \qquad u_e = \frac{At^v L^{\mu}}{s}$$

where $\Gamma_o$ is the strength of the vortex. The Kutta condition requires that the terms in brackets should be zero at the corner and this defines the strength of the vortex as $\Gamma_o = -u_e\pi|z_o|^2/y_o$. However this does not ensure that the flow leaves the corner parallel to the upstream surface, and this is a limitation of the current model. Furthermore the stable location of the vortex has to be defined and this is obtained as the location where $x_o = y_o\sqrt{3}$ so that the vortex is stationary under the influence of its own image vorticity. This is clearly a very simplified model of the vorticity in the separation bubble which is most inaccurate close to the corner, but will suffice for the purpose of this discussion in which we are concerned with the flow well downstream of the reattachment point.

Given this simple model of the steady flow we can study the trajectories of small vortices released into the flow from different locations on the downstream part of the separation bubble. The flow field induced by the vortex and its image is given by the complex potential

$$(9)$$

$$W_m'(Z) = w_m'(z)\frac{dz}{dZ} = \left(\frac{-i\Gamma_m}{2\pi}\left(\frac{1}{z-z_m} - \frac{1}{z-z_m^*}\right)\right)\frac{dz}{dZ}$$

The vortex will be convected by the mean flow and its image and its velocity is given by (Howe 2003) as

$$(10)$$

$$\frac{dZ_m}{dt} = \left(\left(w_o'(z_m) + \frac{\Gamma_m}{4\pi y_m}\right)\frac{dz_m}{dZ} - \frac{i\Gamma_m\zeta''(Z_m)}{4\pi\zeta'(Z_m)}\right)^*$$

For a corner flow we can show that $\zeta''/\zeta' = (\mu-1)/Z_m$ showing that the last term (the Routh correction) is equivalent to placing a vortex of strength $(\mu-1)\Gamma_m/2$ at the corner.

The path of the shed vorticity will depend on its initiation point and it is interesting to investigate its behavior when it is close to the reattachment point as shown in Figure 3. In all examples the perturbation vortex was taken to be $1/10^{th}$ of the strength of the mean flow vortex, and the mean flow vortex will be located at $x_o=0.375$, $y_o=x_o/\sqrt{3}$ so that the reattachment point occurs at $X=1$. Figure 3 shows the paths of the shed vortices released from four points on the downstream side of the separation bubble. The reattachment process is clearly shown and the vortex paths bi-furcate at that point. Note that the paths converge when the vortex comes close to the surface and is propelled upstream under the action of its own image vortex.

Next we will consider the unsteady surface pressure fluctuation caused by a point vortex released into the mean flow just downstream of the separation bubble as illustrated in Figure 2. This can be evaluated from Bournoulli's equation as

$$(11)$$

$$p(X,t) = -\frac{\rho}{2}\left|W_o'(X) + W_m'(X)\right|^2 - \rho\,\mathrm{Re}\left[\frac{dW_m(X)}{dt}\right] + \frac{\rho}{2}\left|W_o'(X)\right|^2$$

which becomes

$$(12)$$

$$p(X,t) = -\rho\,\mathrm{Re}\left[\left(W_o'(X) + \frac{1}{2}W_m'(X)\right)^{\!*} W_m'(X) + \frac{dW_m(X)}{dt}\right]$$

where the second term is

$$(13)$$

$$\mathrm{Re}\left[\frac{dW_m(X)}{dt}\right] = \mathrm{Re}\left[\frac{-\Gamma_m}{\pi}\left(\left(\frac{dz_m}{dt}\right)\frac{1}{x - z_m}\right)\right] = \mathrm{Re}\left[w_m'(x)\frac{dz_m}{dt}\right]$$

which when combined with equation (12) gives

$$(14)$$

$$p(X,t) = -\rho\,\mathrm{Re}\left[\left\{\left(w_o'(x) + \frac{1}{2}w_m'(x)\right)^{\!*}\left|\frac{dz}{dZ}\right|^2 - \frac{dz_m}{dt}\right\}w_m'(x)\right]$$

Using equation (11) then gives (with $dz/dt = (dZ/dt)(dz/dZ)$)

$$(15)$$

$$p(X,t) = -\rho\,\mathrm{Re}\left[\left\{\left(w_o'(x) + \frac{1}{2}w_m'(x)\right)^{\!*}\left|\frac{dz}{dZ}\right|^2 - \left(w_o'(z_m) + \frac{\Gamma_m}{4\pi y_m} - \frac{i(\mu-1)\Gamma_m}{4\pi\mu z_m}\right)^{\!*}\left|\frac{dz_m}{dZ}\right|^2\right\}w_m'(x)\right]$$

At large distances from the corner when the vortex is relatively strong and close to the surface we can approximate $w_o'(z_m) = w_o'(x)$ and $dz/dZ = dz_m/dZ$ and obtain the approximate pressure signature

$$(16)$$

$$p(X,t) = -\rho\,\mathrm{Re}\left[\left(\frac{1}{2}w_m'(x) - \frac{\Gamma_m}{4\pi y_m} + \frac{i(\mu-1)\Gamma_m}{4\pi\mu z_m}\right)^{\!*}\left|\frac{dz_m}{dZ}\right|^2 w_m'(x)\right]$$

However for weaker vortices that are further from the surface the terms that are of order $\Gamma_m^2$ will be small compared to terms of order $\Gamma_m$ and so we need only include terms that are linear in vortex strength giving

$$p(X,t) = -\rho \operatorname{Re}\left[ \left\{ \left( w_o'(x) \right)^{\cdot} \left| \frac{dz}{dZ} \right|^2 - \left( w_o'(z_m) \right)^{\cdot} \left| \frac{dz_m}{dZ} \right|^2 \right\} w_m'(x) \right]$$

(17)

We will treat these two cases separately and compare the results with measurements of surface pressure, however it is worth noting that the non linear terms will dominate if

(18)

$$|w_o'(x_m)| << \frac{\mu \Gamma_m x_m^2}{8\pi(\mu-1)y_m^3}$$

which will always be the case at very large distances from the corner where $x_m >> y_m$.

*Stronger vortices*

For the stronger vortices at large distances from the corner we can ignore the Routh correction and reduce equation (16) to

(19)

$$p(X,t) = -\rho \left( \frac{\Gamma}{2\pi} \right)^2 \left( \frac{y_m^2 - ((x - x_m)^2}{(y_m^2 + (x - x_m)^2)^2} \right) \left| \frac{dz_m}{dZ} \right|^2$$

This result shows how the pressure pulse is a non linear function of the vortex strength and its peak pressure depends on the distance of the vortex from the surface. If the vortex follows a streamline the peak amplitude of the pulse, which occurs when $x=x_m$, will decay with downstream distance as $|dz_m/dZ|^2$ which is $\sim \mu^2 X^{2\mu-2}$. However the influence of the separation bubble, other vorticity and the Routh correction will cause the vortex to follow a different path, even at large distances from the corner. Figure 4(a) shows an example calculation of the downstream path of the vortex compared to the corner flow stream lines. This lift up is caused by the Routh correction and while it is a small effect, it has a significant impact over large distances. To confirm this Figure 4(b) gives the path of the vortex if the Routh correction is not included. In this case the vortex follows the corner flow streamlines more closely and deviates only because of the influence of the separation bubble and its image, which causes a slight drift towards the surface. This feature is a limitation of the model, and it is unlikely that the Routh correction is more important in a real flow than the influence of additional vorticity being shed from the separation bubble.

Figure 5(a) shows the pressure time history at a point as a function of the normalized time scale (note: it will be shown below that this translates between the mapped domain and the physical domain). It is interesting that this pulse has two negative side lobes on either side of the main peak, which is consistent with the surface pressure correlation functions measured by Awasthi *et al*(2013).

*Weaker Vortices*

When the individual vortices are very weak the pressure pulse will be given by equation (17) which reduces to

(20)

$$p(X,t) = \frac{\Gamma_m y_m |w_o'(x)| \Delta}{\pi((x - x_m)^2 - y_m^2)} \left| \frac{dz}{dZ} \right|^2 \qquad \Delta = \frac{2(1-\mu)y_m^2}{\mu x_m^2}$$

The pressure pulse for the linear interaction is shown in Figure 5(b) and is seen to be quite different than the non linear pulse in Figure 5(a). In this case there are no negative loops and the pressure pulse decays monotonically from its peak value. This is inconsistent with the correlation functions of the surface pressure measured by Awasthi *et al*(2013) and so it seems unlikely that this mechanism is important in the real flow.

## V. Surface Pressure Spectra

The experimental results of Awasthi *et al.* (2013) showed that the surface pressure spectra downstream of the separation bubble were self similar. In this section we will investigate this theoretically by using the strong vortex model given above.

If we specify $x_o(t)-x=u_c t$ as the local time dependence of the vortex position in the $z$ plane and take the Fourier transform of equation (19) with respect to time we obtain

$$(21)$$

$$p(\omega) = \frac{-i\omega\rho\Gamma_m^2}{4u_c^2}\left|\frac{dz_m}{dZ}\right|^2 e^{-|\omega y_m/u_c|}$$

The power spectra of the surface pressure fluctuations is defined as

$$\Phi_{pp}(\omega) = \frac{\pi}{T}Ex\left[|p(\omega)|^2\right]$$

and since the vortex height above the surface is a random variable we can evaluate the spectrum using the probability density function of the vortex height $P(y_m)$, so

$$(22)$$

$$\Phi_{pp}(\omega) = \frac{\pi}{T}\int_0^\infty \left[|p(\omega)|^2\right]P(y_m)dy_m$$

If we choose the probability density function as $P(y_m)=C(y_m)^\kappa \exp(-y_m/h_e)$ where $C$ is a scaling constant given by $C=h_e^{-(\kappa-1)}/\Gamma(\kappa+1)$ then we obtain

$$(23)$$

$$\Phi_{pp}(\omega) = \left(\frac{\omega\rho\Gamma_m^2}{4u_c^2}\left|\frac{dz_m}{dZ}\right|^2\right)^2\frac{\pi C}{T}\int_0^\infty y_m^\kappa e^{-(1/h_e+|\omega/u_c|)y_m}dy_m$$

This is a simple integral to evaluate and yields

$$(24)$$

$$\Phi_{pp}(\omega) = \frac{(\omega h_e/u_c)^2 F(X)}{(1+(\omega h_e/u_c))^{\kappa+1}} \qquad F(X) = \frac{\pi}{T}\left(\frac{\rho\Gamma_m^2}{2h_e u_c}\left|\frac{dz_m}{dZ}\right|^2\right)^2$$

Finally we note that this analysis has been carried out in the $z$ plane and we need to relate the results to the physical flow variables (donated by upper case letters). Given the relationship (7) we have when $X>>H_e$

$$x+ih_e = (s/L^\mu)(X+iH_e) \approx (s/L^\mu)(X^\mu+i\mu H_e X^{\mu-1}+....)$$

so $h_e=\mu(s/L^\mu)H_e X^{\mu-1}$ and

$$u_c = \left(\frac{dx}{dX}\right)U_c = \mu\left(\frac{s}{L^\mu}\right)X^{\mu-1}U_c$$

so $u_c/h_e = U_c/H_e$ and $u_c h_e = U_c H_e (dx/dX)^2$. The scaling in (23) is then written as

(25)

$$\Phi_{pp}(\omega) = \frac{(\omega H_e/U_c)^2 F(X)}{(1+(\omega H_e/U_c))^{\kappa+1}} \qquad F(X) = \frac{\pi}{T}\left(\frac{\rho\Gamma_m^2}{2H_e U_c}\right)^2$$

It is interesting to compare these results with the measurements of Awasthi *et al* (2013) for the flow over a forward facing step. The geometry for the step is different than the corner and the mean flow streamlines do not move off the surface as quickly as those shown in Figure 4 at large distances downstream of the step. However the mechanisms of flow separation are expected to be similar. Awasthi *et al* (2013) scaled the flow spectra in a self similar manner assuming a linear model and it is interesting to contrast their result with scaling based on the non linear model described here. First we will consider the high frequency asymptote of the measured self similar spectra given by Awasthi *et al.* (2013) and compare it to the model given by equation (25). The fit to the measured self similar spectrum is given in Figure 6 where we have used $\kappa=11/3$ and adjusted the peak frequency so that the slope of the curve is -1 at the non dimensional frequency $f/f_{peak}=1$ as in the original plot. The agreement is remarkably good across the entire spectrum. We can also use the Awasthi *et al* (2013) data to define the characteristic of the peak frequency and amplitude as a function of distance downstream as shown in Figures 7 and 8. The peak in the measured pressure spectrum gives $F(X)\sim X^{-2}$ or $H_e U_c \sim X$. The scaling of the measured ridge frequency shown in Figure 8 suggests that $U_c/H_e \sim X^{-1/3}(U_c/z_0)h/U_\infty \sim (x/h)^{-1/3}$ and we can combine these results to suggest $U_c \sim X^{1/3}$ and $H_e \sim X^{2/3}$. The convection velocity is therefore slowly increasing, and the structures move away from the wall as shown in Figure 4. If the vortex is convected along a streamline for a corner then we would expect $H_e \sim X^{2/3}$ and for a step we would expect that $H_e$ tends to a constant if there were no additional effects. The impact of additional vorticity may alter these simple scaling laws and give a scaling for $H_e$ that lies between these two extremes, but the measurements suggest that the vorticity is following the streamline of the corner flow. It would appear from these results that this model, which is based on three unknown scaling parameters $\kappa$, $U_c$, and $H_e$ is remarkably consistent with the measurements. It also allows us to specify the probability of the height of the vortex structure as shown in Figure 9. This has a clearly defined peak and indicates that vortices are concentrated closer to the wall than in the outer boundary layer. It is interesting to note that the spectral shape is determined in the model by both the characteristic shape of the surface pressure pulse from the passing vortex and the probability of the height of the vortex structure above the surface, which determines the pressure pulse lengthscale and the high frequency asymptote of the surface pressure spectrum.

## VI. Acoustic Radiation

We will now consider the sound radiation for a forward facing 90° step. We can evaluate the acoustic radiation from the step flow using Curle's theorem as defined in equation (1). However we are most interested in the power spectrum of the acoustic pressure at large distances from the surface and so we will consider the Fourier transform of equation (1) with respect to time. If the viscous shear stress on the surface is small then we obtain

(26)

$$p(\mathbf{x},\omega) = -\int_S p(\mathbf{y},\omega)\frac{\partial G_\omega(\mathbf{x}|\mathbf{y})}{\partial n}dS(\mathbf{y}) + \int_V T_{ij}(\mathbf{y},\omega)\frac{\partial^2 G_\omega(\mathbf{x}|\mathbf{y})}{\partial y_i \partial y_j}dS(\mathbf{y})$$

We can use the far field approximation for the frequency domain Greens function that satisfies the non penetration boundary condition on the surface upstream of the step so

$$G_\omega(\mathbf{x}\,|\,\mathbf{y}) = \left(\frac{e^{ikr_o - ikx_1 y_1/r_o - ikx_3 y_3/r_o}}{2\pi r_o}\right)\cos(kx_2 y_2\,/\,r_o)$$

where $r_o$ is the distance from the inside corner of the step to the observer and the step span is aligned with the $y_3$ axis. Also we note that the acoustic space variables are related to the variables in the complex plane as $y_1 = X$ and $y_2 = Y$. The acoustic wavenumber is defined as $k = \omega/c_o$.

The far field sound then is given by the sum of the two terms in equation (17). The first term is the contribution from the surface pressure and the second is the contribution from quadrupole sources. As will be shown below the surface pressure fluctuations are dominated by the region close to the upper corner of the step and so may be treated as a compact acoustic source. The surface integral of the pressure can then be replaced by the net force per unit length on the surfaces $F_i$ and is defined (for an observer in the plane $x_3 = 0$) as

(28)

$$p_s(\mathbf{x},\omega) = \frac{ke^{ikr_o}}{2\pi r_o}\int_{-\infty}^{\infty}\left(\frac{ix_1}{r_o}\cos(khx_2\,/\,r_o)F_1(\mathbf{y},\omega) + \frac{x_2}{r_o}\sin(khx_2\,/\,r_o)F_2(\mathbf{y},\omega)\right)dy_3$$

The point of action of the force has been chosen as the top corner of the step.

The second term represents the quadrupole source terms and these can be defined as

(29)

$$p_q(\mathbf{x},\omega) = \frac{e^{ikr_o}}{2\pi r_o}\int_V T_{ij}(\mathbf{y},\omega)\frac{\partial^2}{\partial y_i \partial y_j}\left(\cos(ky_2 x_2\,/\,r_o)e^{-ikx_1 y_1/r_o}\right)dV$$

In the following sub sections we will discuss the relative importance of these two source terms.

## A. The Unsteady Loading

In order to calculate the sound radiation from the surfaces we need to model the unsteady loading. For a two dimensional vortex model this is customarily carried out using the vortex impulse method (Saffman (1992)) or by using Howe's formula (Howe (2003)). Both methods assume a flow over a finite body and impose a no slip boundary condition on all surfaces. The no slip boundary condition is not part of an ideal flow model and so is a limitation of both methods. This can be an issue for the vortex impulse method, but Howe's formula minimizes this potential problem, and the error is zero if the no slip condition is satisfied by a thin layer of vorticity on the surface providing the vortex lines are co planar to the surface. In the corner flow problem described above the surfaces are of infinite extent and so neither method can be applied directly. However if we modify the surface a large distances from the corner and any associated separated flow we can use Howe's method to obtain the force on the surface.

Howe's formula gives the unsteady surface loading as the volume integral

(30)

$$F_i = \int_V \rho(\boldsymbol{\omega}\times\mathbf{v}_{rel}).\nabla\Phi_i\,dV$$

where $\omega$ is the vorticity in the flow, $\mathbf{v}_{rel}$ is the velocity relative to the body and $\Phi_i$ is the potential of an ideal flow over the same body (at rest) that has unit velocity in the $i$ direction at infinity. For a line vortex with circulation $\Gamma_m$ at $Z_m$ in an ideal two dimensional flow described by the complex velocity potential $W(Z)$ we can write Howe's formula for the force on the body per unit span as

$$(31)$$

$$f_i = \text{Re}\left[i\rho\Gamma_m\left(\frac{dZ_m}{dt}\right)W_i'\right]$$

where $W_i$ is the complex potential of the flow in the $i$ direction with unit velocity at infinity. For the corner flow problem discussed above we cannot define $W_i$ because the flow does not become uniform at infinity. However if we modify the surface as illustrated in Figure 10 for two different flow directions then $W_i$ can be defined and the force in each direction can be calculated. Providing that the additional corners added to the surface are sufficiently far from the surface that they do not influence the flow in the corner and the vorticity close to the corner acts locally on the surface, then the modified surface will be a good approximating to the ideal corner. The immediate conclusion from this model is that the flow in the vicinity of the corner is the same in both cases, so the unsteady loading on each surface will be the same. Therefore, for the step problem discussed above, the forces $F_1$ and $F_2$ in equation (28) are equal.

We need to verify that the flow scales correctly and the force is independent of the location of the appended surface. Taking the surface shown in Figure 10(a) the complex potential $W_i$ can be defined so

$$(32)$$

$$W_1' = \frac{dz}{dZ} = \frac{(s+z)^{\alpha/\pi}}{z^{\alpha/\pi}}$$

where $s$ is sufficiently large that $z<<s$ in the region of the vortex. The convection velocity of the vortex is given by equation (11) and so the unsteady loading will be

$$(33)$$

$$f_1 = \text{Re}\left[i\rho\Gamma_m\left(\left(w_o'(z_m)+\frac{\Gamma_m}{4\pi y_m}\right)-\frac{i\Gamma_m\zeta''(Z_m)}{4\pi\left(\zeta'(Z_m)\right)^2}\right)^*\left|\frac{dz_m}{dZ}\right|^2\right]$$

(note: $\zeta'=dz/dZ$). In this equation we see immediately that only the imaginary part of the convection velocity will contribute. This implies that there will only be an unsteady load if the vortex moves normal to the streamlines as expected from equation (30). The mean flow $w_o'$ is given by equation (11) and since only the imaginary part of this term is important, only the motion of the vortex that is induced by the separation bubble and the Routh correction in equation (33) will affect the loading. Both these terms are proportional to the square of the vortex strength which on the basis of equation (9) scales on $u_e$ and $u_e|dz_m/dZ|=U_m$ represents the flow speed at the vortex in the physical plane. We then have

$$(34)$$

$$f_1 = \rho U_m^2 |z_o| \text{Re}\left[\left(\frac{i\Gamma_o\Gamma_m y_o}{\pi u_e^2 |z_o|(z_m-z_o)(z_m-z_o*)}\right)+\frac{\Gamma_m^2\zeta''(Z_m)}{4\pi u_e^2 |z_o|\left(\zeta'(Z_m)\right)^2}\right]$$

This result can be recast in terms of the non dimensional circulation $\Gamma_o/u_e|z_o|$ which is independent of the scale $s$ and it follows that the first term in [] <???above is non dimensional. The second term can also be reduced by noting that in the vicinity of the step $z_o=sZ_o^\mu$ and $dz_m/dZ=\mu sZ_m^{(\mu-1)}$ so

$$\frac{\Gamma_m^2 \zeta''(Z_m)}{4\pi u_e^2 |z_o|(\zeta'(Z_m))^2} = \left(\frac{\Gamma_m^2}{u_e^2 |z_o|^2}\right) \frac{(\mu-1)|z_o|}{4\pi Z_m (dz_m/dZ)} = \left(\frac{\Gamma_m^2}{u_e^2 |z_o|^2}\right) \frac{(\mu-1)|Z_o|^\mu}{4\pi\mu Z_m^\mu}$$

which is also independent of the scale $s$. We have therefore shown that the modified surface does not affect the loading providing the vortex moves only under the influence of the flow local to the corner.

One of the features of equation (34) is that the loading is caused by the interaction of the vorticity in the separation bubble with the shed vortex, and the contribution from the Routh correction. The physics of the model suggests that the loading is generated by the rotation of the shed vortex around the separation bubble, and it is this interaction that controls the sound radiation. However we have assumed above that the separation bubble has constant circulation and does not move under the influence of the shed vortex. This cannot be the case and we must include the possibility of the separation bubble being moved by the shed vortex. The additional loading is readily obtained from (34) by interchanging the vortex positions giving

(36)

$$f_1^{(o)} = \rho U_o^2 |z_o| \text{Re}\left[\left(\frac{i\Gamma_o \Gamma_m y_m}{\pi u_e^2 |z_o|(z_o - z_m)(z_o - z_m^*)}\right) + \frac{\Gamma_o w_v'(z_o)}{u_e^2 |z_o|}\right]$$

The vortex interaction terms in (34) and (36) tend to cancel and if $\Gamma_m << \Gamma_o$ they are insignificant in comparison to the second term in (36). The second term in (36) represents the motion of the separation bubble caused by the developing flow, as described in section III, and $w_v$ is defined by equation (4). However it is at this point that the simplified model starts to become invalid because the dynamic effects of the shed vorticity on the Kutta condition and the motion of the separation bubble is beyond the simple modeling approach being used here. The analysis has shown however that these effects dominate the unsteady loading and the shed vorticity by itself is not the issue. This leads to the conclusion that it is the development and motion of the separation bubble that drives the unsteady load and radiated sound.

### B. Acoustic Surface Sources

We can combine the results above with the acoustic analysis to give the sound radiation from the surface. For a forward facing step we can take the forces on each face of the step to be the same and, in the acoustically compact limit, to act as a point force on the corner of the step. The magnitude of the force remains as an unknown and has to be estimated. Combining the results above we obtain the far field spectrum for a forward facing step as

(37)

$$S_{pp}(\mathbf{x},\omega) = \frac{k^2 S_{ff}(\omega)}{(2\pi r_o)^2} \left|\frac{ix_1}{r_o}\cos(khx_2/r_o) + \frac{x_2}{r_o}\sin(khx_2/r_o)\right|^2$$

This result scales on $k^2$ and so can be regarded as a dipole. At low frequencies the first term in the brackets will dominate and the directionality will depend on $x_1/r_o$, which is an axial dipole. At high frequencies both terms will be important and interfere to give a more complex directionality, but the dipole scaling on the wavenumber is consistent at all frequencies. If the spectrum of the fluctuations $S_{ff}(\omega)$ scales on flow speed and some fixed length scale, then the dipole scaling will give overall source levels that scale on the sixth power of the flow speed and $M^2$, as expected from a dipole.

### C. Volume Sources

The volume sources will depend on the Lighthill stress tensor that is particularly difficult to model. However we can resort to known solutions for sound radiation from distributions of point vortices in the free field to assess the magnitude of this term. The problem of sound radiation from two point vortices rotating about each other was addressed by Powell (1963). The final result gives the acoustic far field as

(38)

$$p_q = \frac{k^2 \Gamma_o \Gamma_m R e^{ikr_o}}{8\pi r_o} \delta(\omega - 2\Omega)$$

where $\Gamma_o$ and $\Gamma_o$ are the strengths of the two vortices separated by a distance $R$, and $\Omega$ is the angular speed of their self induced motion about their centroid. Comparing this result to equation (28) for the dipole term we note that the order of magnitude of the quadrupole source is ~$kR$ less than the surface sources. This is typical of a quadrupole source and in general we can discard this term if $kR$ is small. Since in general the sound radiation will be dominated by sources close to the step corner where $R<<h$ then it is a reasonable approximation to ignore the quadrupole term.

**D. Comparison with Experimental Data**

It is not possible to directly compare the model described above with the far field sound because the spectrum of the unsteady loading $S_{ff}(\omega)$ is unknown. However by fitting a single amplitude to the data at one observer angle it should be possible to predict the spectra at different observer angles. By comparison with the experimental measurements of Catlett *et al* (2014) it has been found that the best fit to the data is given by

(39)

$$S_{ff}(\omega) = \frac{3 \times 10^5}{\left(1 + (\omega h / U_\infty)^2\right)^{7/3}}$$

Given these parameters the spectral shape is well predicted for all frequencies and angles as shown in Figure 11. Note that the high frequency dip is well predicted and that the axial dipole characteristic is apparent at low frequencies.

## V. Conclusion

In this paper we have considered a simple two dimensional model of the separated flow downstream of a corner and modeled the pressure fluctuations on the surface, the unsteady loadings, and the sound radiation. We have chosen to model the flow by a separation bubble that periodically sheds vorticity.

We have shown that the characteristics of unsteady surface pressure are well characterized by this simple model and proportional to the square of the circulation in the shed vorticity. The linear interaction of the mean flow with the shed vorticity has a second order effect on the surface pressure which can be ignored at large distances downstream from the separation bubble. The calculated surface pressure spectrum was compared to measurements and excellent agreement was found by matching three modeling parameters to the data, the convection velocity $U_c$, the mean height of the shed vorticity above the surface $H_e$, and the coefficient $\kappa$ which describes the probability function of the height of the shed vortex above the surface.

We also considered the sound radiation and unsteady loading on the corner. It was shown that, regardless of the details of the flow, the loading on each surface of the corner was the same and this controls the directionality of the far field sound. Comparisons were made with measured far field sound

spectra with excellent agreement. The role of the shed vorticity on the unsteady loading was also investigated and it was concluded that it has a second order effect. The primary source of the unsteady loading is determined by the unsteady growth and motion of the separation bubble which will depend on its interaction with the corner and the application of the Kutta condition. A more detailed model of the flow in this region is required to characterize the unsteady flow correctly, and three dimensional effects must be included to properly identify the mechanisms taking place.

## Acknowledgments

## References

Awasthi M., Bryan. B., Devenport W., Glegg S., 2013, , "Sound Radiation from Rounded Steps and Gaps", 19th AIAA/CEAS Aeroacoustics Conference, Berlin, June 2013

Catlett, M.R., Devenport, W. and Glegg, S., 2014, "Sound from Boundary Layer Flow over Steps and Gaps", Journal of Sound and Vibration 333 (2014), pp. 4170-4186

Cherry, N.J., Hillier, R., and Latour, M.E.M.P, 1984, Unsteady measurements in a separated and reattaching flow, J. Fluid. Mech, vol 44, pp13-46

Howe, M. S. 2003 "Theory of Vortex Sound." Cambridge University Press.

Kiya, M., and Saski, K., 1983, Structure of turbulence separation bubble, J. Fluid Mech. Vol 137, pp83-113

Ji M. and Wang M., 2010, "Sound Generation by Turbulent Boundary Layer Flow over Small Steps", Journal of Fluid Mechanics, vol. 654, pp. 161-193.

Pullin, D.I., 1978 The large scale structure of unsteady self similar rolled-up vortex sheets, J. Fluid. Mech., vol 88(3), pp 401-430

Saffman 1992, Vortex Dynamics, Cambridge University Press

Slomski, J. F. "Numerical Investigation of Sound from Turbulent Flow over a Forward Facing Step." American Institute of Aeronautics and Astronautics 17 (2011)
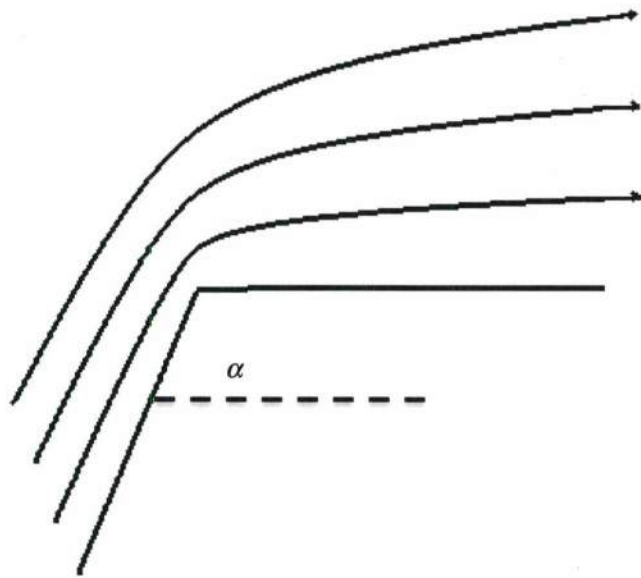
Figure 1: The geometry used for the corner flow
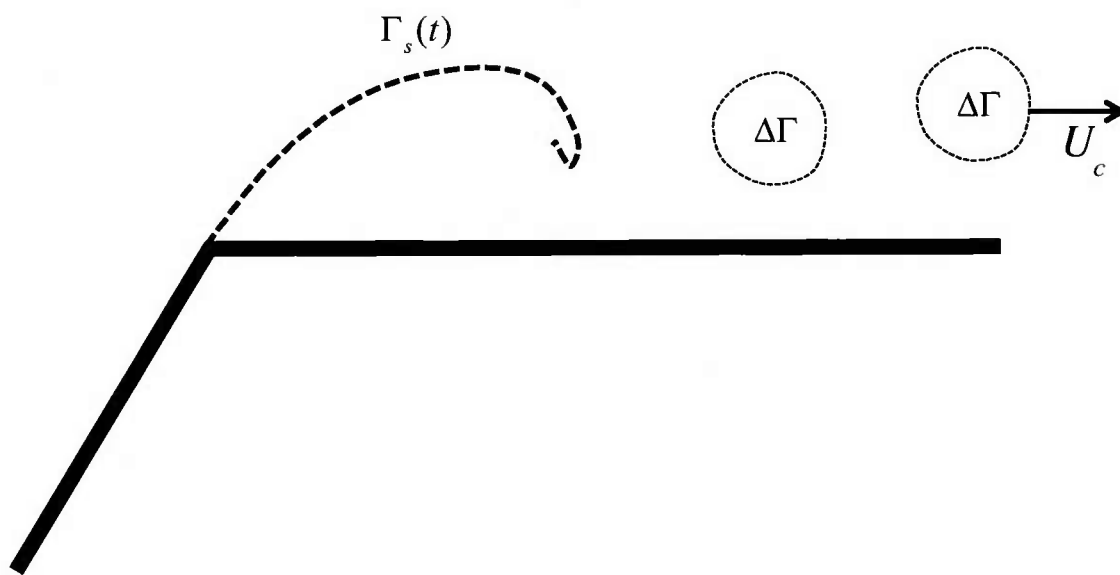
Figure 2: The model of a vortex sheet periodically shedding discrete vortices
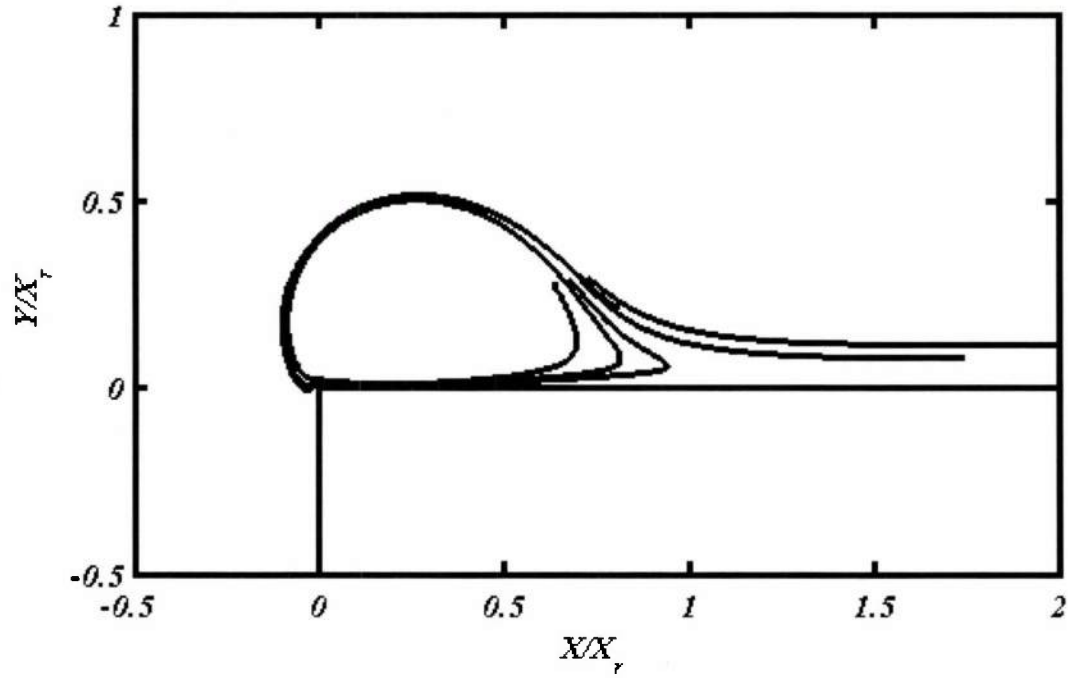
Figure 3: Vortex trajectories for vortices initiated at $z=z_o+x_o, z_o+1.1x_o, z_o+1.15x_o, z_o+1.2x_o$ showing the reattachment point location and the location of the steady state separation bubble. The Kutta condition is satisfied at the corner for the mean flow only.
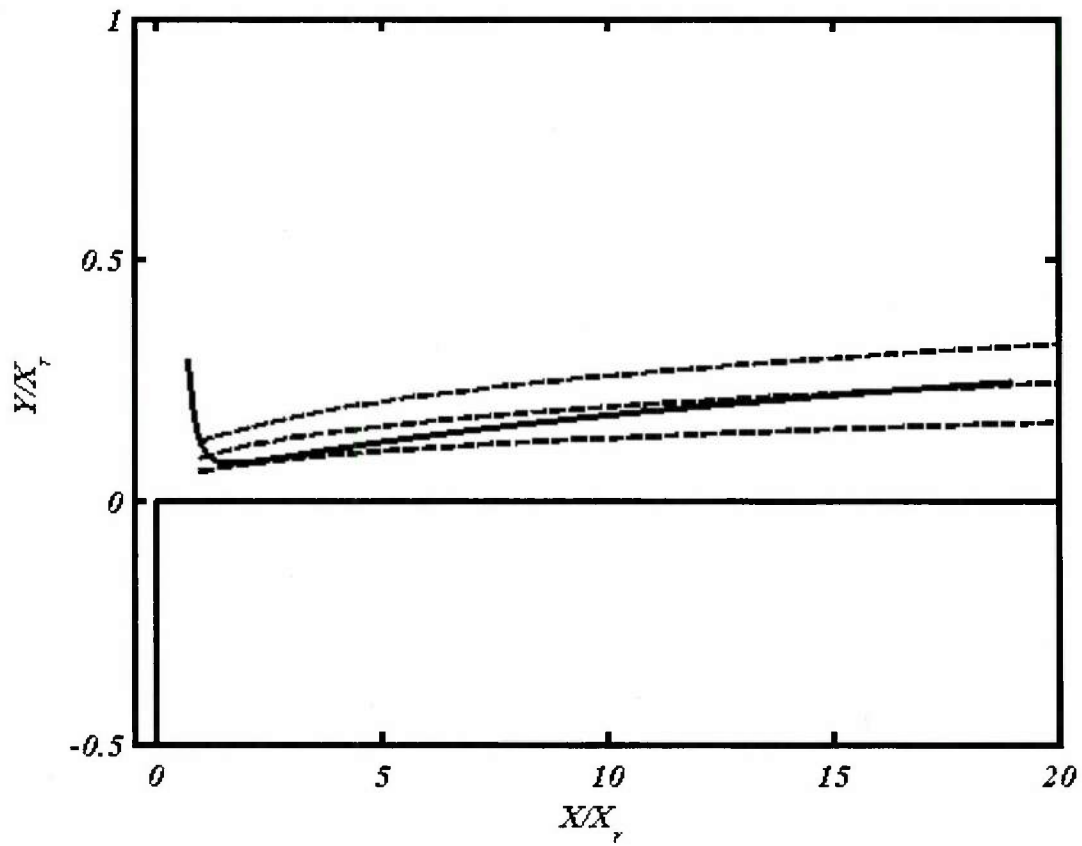
Figure 4(a): The trajectory of vortex in the downstream direction under the action of the mean flow and the vorticity in the separation bubble. Solid line is the vortex trajectory, dashed lines are the streamlines of the flow (includes Routh correction).
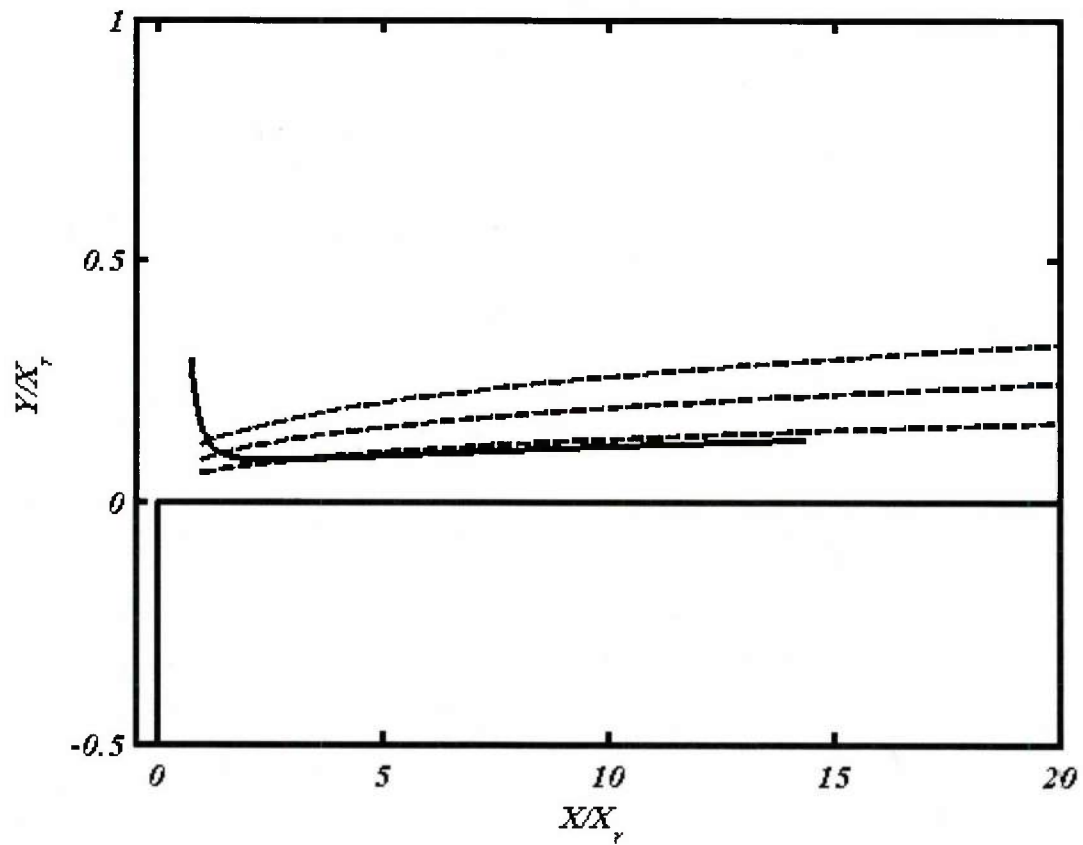
Figure 4(b): The trajectory of vortex in the downstream direction under the action of the mean flow and the vorticity in the separation bubble. Solid line is the vortex trajectory, dashed lines are the streamlines of the flow (without Routh correction).
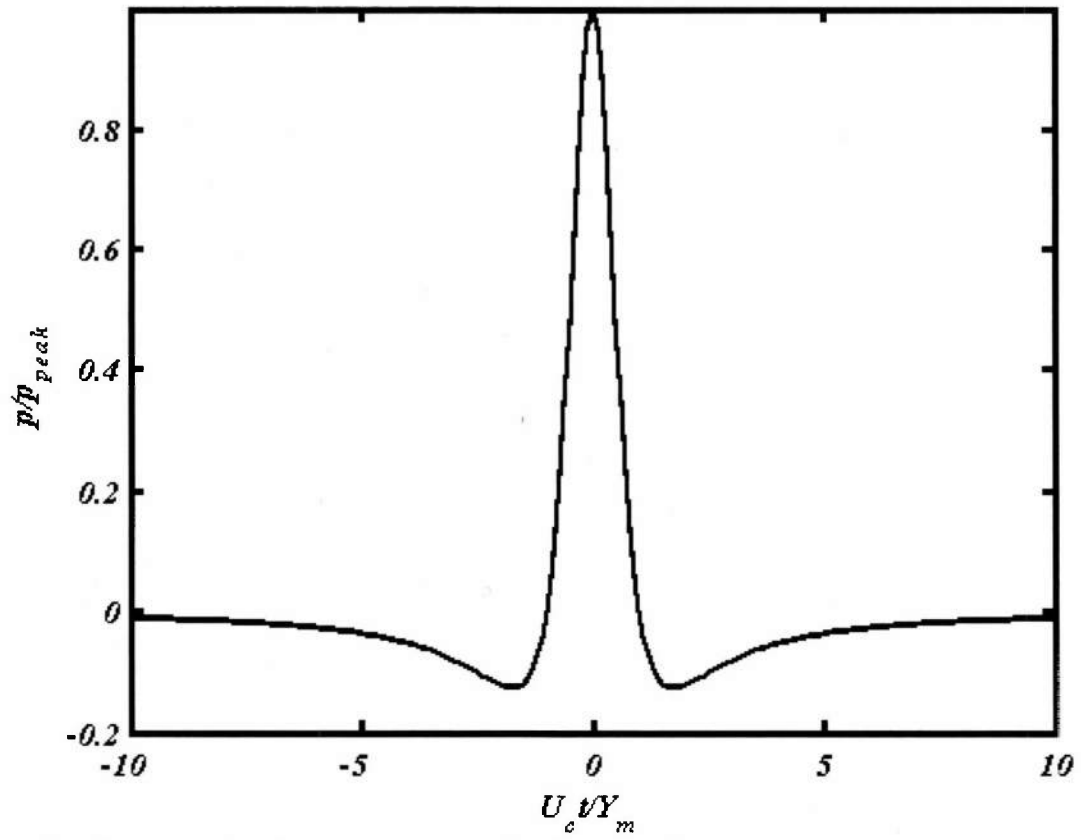
Figure 5(a): The normalized surface pressure pulse caused by the passage of a strong vortex
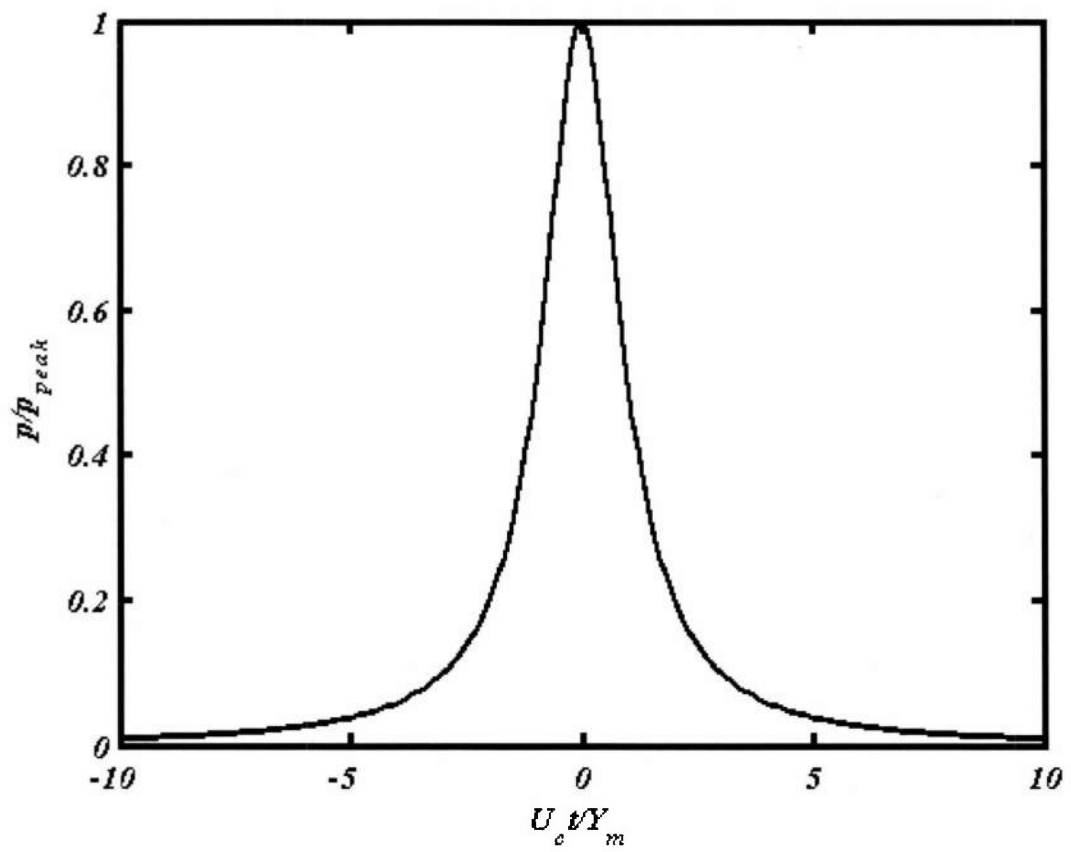
Figure 5(b): The normalized surface pressure pulse caused by the passage of a weak vortex
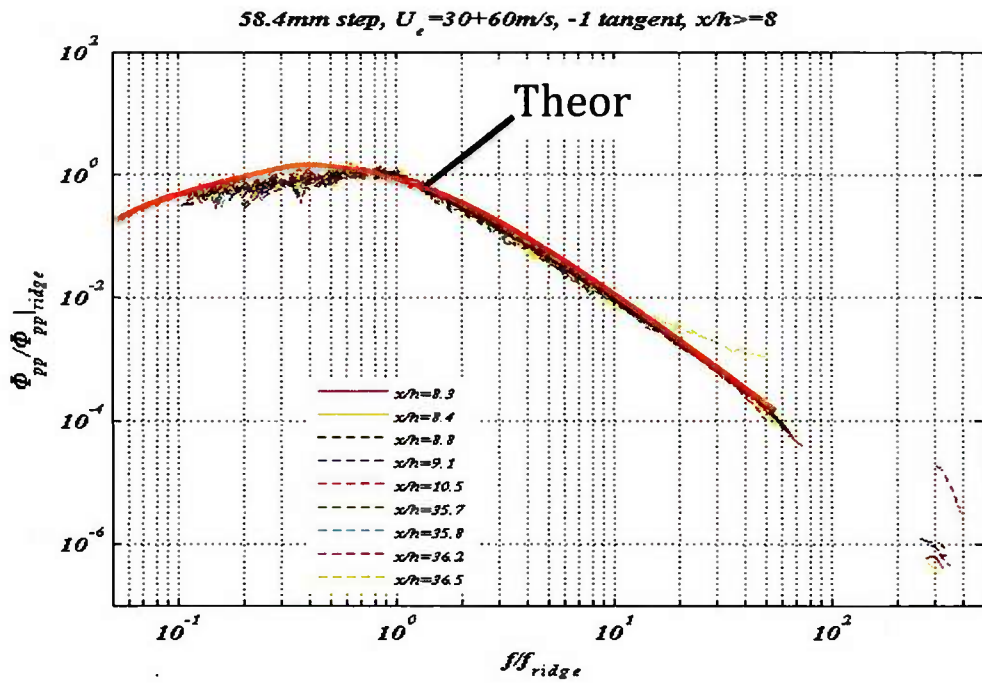
Figure 6: The self similar surface pressure spectra downstream of the separation zone compared to the theoretical estimate
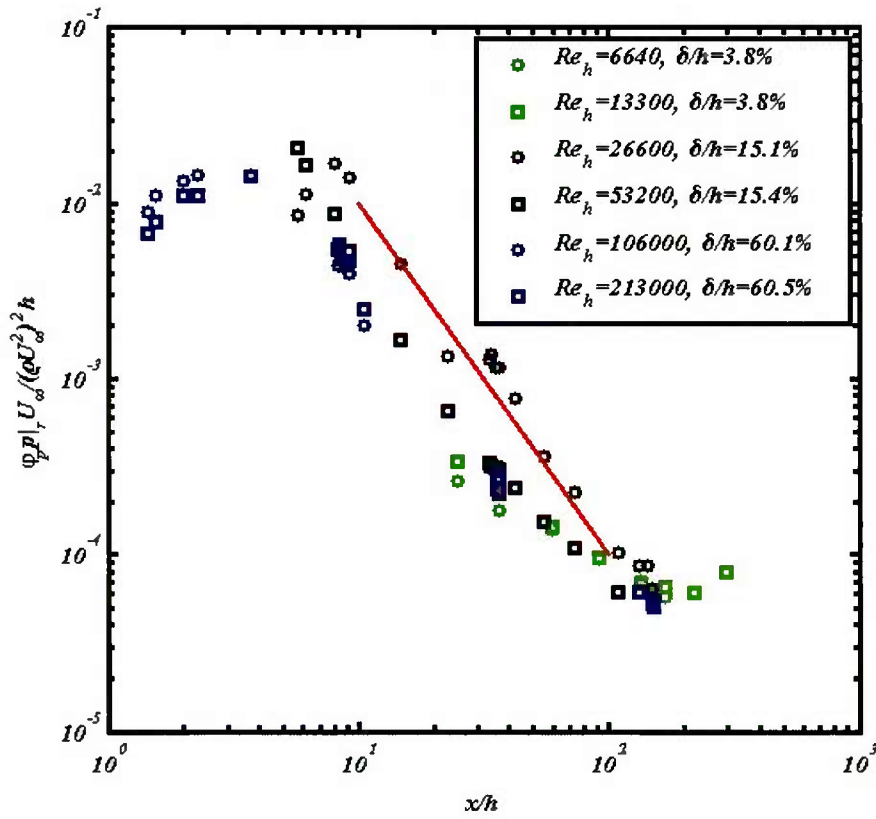
Figure 7: The experimental results of Devenport et al(2013) showing the decay of the mean square surface pressure as a function of distance downstream. The line shows the scaling based on $X^{-2}$.
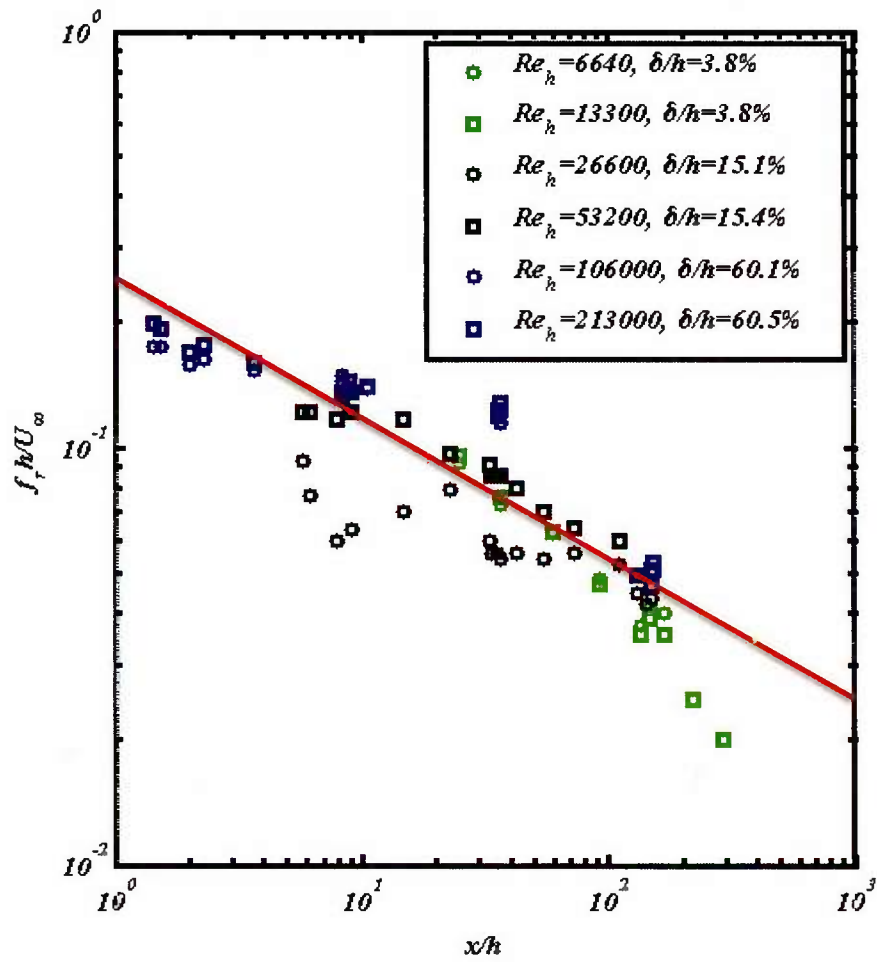
Figure 8: The experimental results of Devenport et al(2013) showing the decay of the peak frequency in the surface pressure spectrum as a function of distance downstream. The line shows the scaling based on the slope of $X^{1/3}$
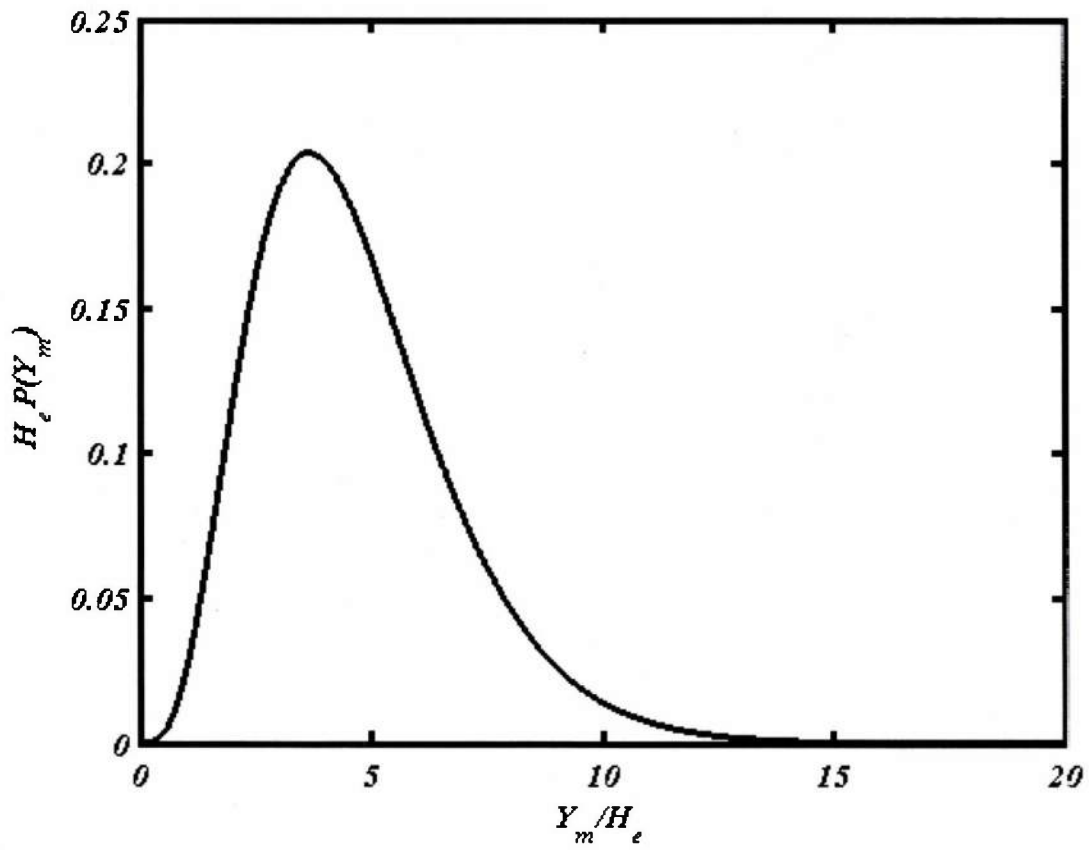
Figure 9: The probability density function for the location of vortices above the surface.

Flow in the region of the corner is the same in both cases
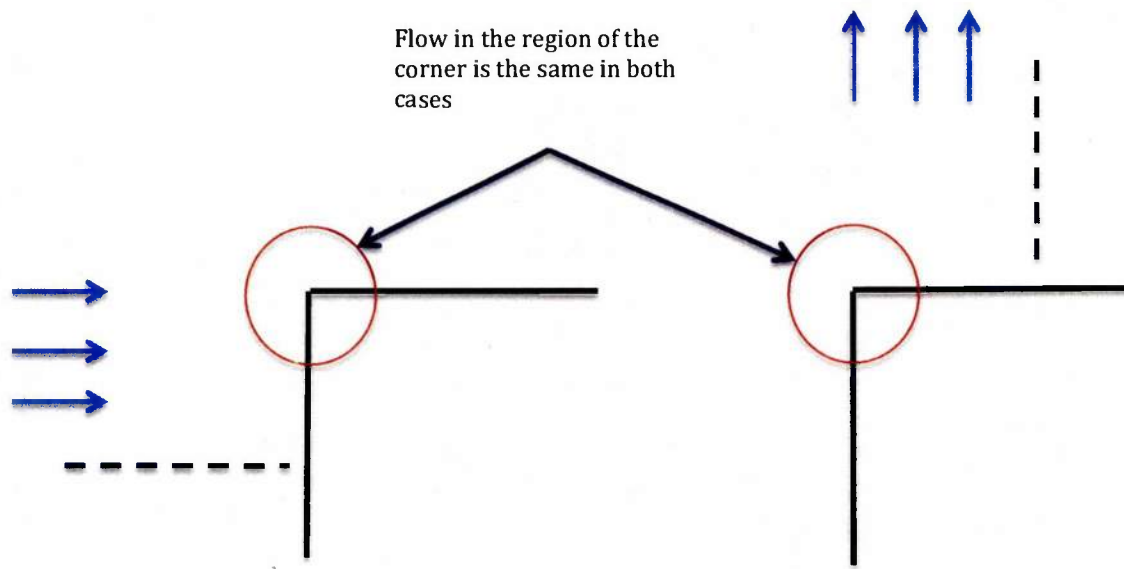
Figure 10: Showing the modified flow around a corner required for the unsteady loading estimate.
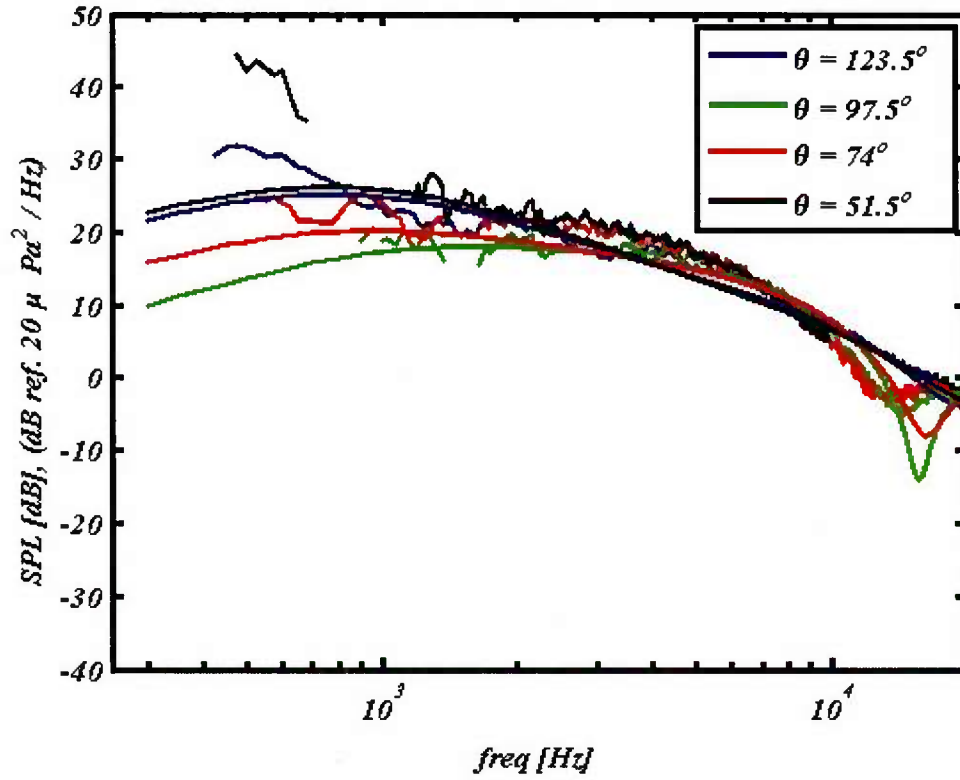
Figure 11: The predicted spectra compared to measurements made by Catlett *et al*(2014)

# Noise Radiation from a Cylindrical Embossment Immersed in Turbulent Boundary Layer Flow

Benjamin S. Bryan[5] and Stewart Glegg[6]
*Florida Atlantic University, Boca Raton, FL 33431*

Manuj Awasthi[7] and William Devenport[8]
*Virginia Tech, Blacksburg, VA 24060*

**This paper will consider the flow around a three dimensional cylindrical embossment of very low aspect ratio mounted on a plate. The sound radiation from this flow will be predicted using the theory outlined in Glegg *et al* (2014) along with RANS simulation results. Predictions will then be compared with wind tunnel measurements. Simulations show that the cylinder exhibits a separation zone on the leading half of the cylinder. The predictions of the far field sound shows a clearly defined directionality that is similar to an axial dipole at low frequencies.**

## I.    Introduction

THE noise from protrusions and discontinuities on flat surfaces is important in both aeroacoustic and hydroacoustic applications. Underwater vehicles and aircraft with bluff bodies mounted on their exterior surfaces will generate additional noise which can be a concern in applications where airframe or vehicle surface noise is important.

### A. The Sound from Flow Over Steps

Farabee and Casarella (1986) examined pressure fluctuations on both forward and backward facing steps. Experiments were performed in an anechoic wind-tunnel and pressure fluctuations were measured using flush mounted microphones. The Reynolds number for the forward-facing step was $Re_h = 2.1 \times 10^4$ and $Re_h = 2.3 \times 10^4$ for the backward facing step where $h = 1.27cm$. Hot-wire probes were used to measure velocities and determine reattachment lengths. The reattachment lengths were 3-4 step heights and 6-8 step heights for the forward and backward steps respectively. RMS measurements of surface pressure fluctuation at the reattachment point were up to 10 times greater than those in equilibrium flow for the forward step and 5 times greater for the backward step. RMS pressure fluctuations decayed with increasing downstream distance from the reattachment point, but were still greater than equilibrium as far as 15 step heights downstream. The flow had still not returned to equilibrium at 72 step heights downstream. In the forward-facing step significant fluctuations occur upstream of the step as well. The

---

[5] Graduate Student, Dept. of Ocean and Mechanical Engineering, and AIAA Student Member.
[6] Professor, Dept. of Ocean and Mechanical Engineering, and AIAA Associate Fellow.
[7] Graduate Student, Department Aerospace and Ocean Engineering, and AIAA Student Member.
[8] Professor, Department Aerospace and Ocean Engineering, and AIAA Associate Fellow.

large pressure fluctuations in the vicinity of the steps were attributed to the low-frequency content of the pressure spectrum. The conclusion drawn was the importance of the upstream flow. The reluctance of the flow to return to equilibrium shows that any perturbations in the upstream flow can have significant influence in the downstream region.

Farabee and Zoccola (1998) continued Farabee's earlier work using the same parameters as in Farabee and Casarella (1986) except that in addition to the backward step having $h = 1.27$ cm, two forward step heights were tested. The forward steps had heights $h = 0.76$ cm and $h = 1.4$ cm. Also a second flow speed was used. The two flow speeds were $U = 25.5$ m/s and $U = 40.7$ m/s. In this study directional microphones were used to measure far-field sound radiation from the steps. No radiation was detected from the backward facing step. Both of the forward steps showed significant far-field radiation. It was shown that the sound radiation was effected only slightly by the change in step height. However, the far-field spectra were shown to be uniformly dependent on the free stream velocity.

Catlett (2010) measured far-field sound radiation from flow over several configurations of forward-facing steps, backward steps, and gaps. Four directional microphones were placed over the step at different angles from the vertical. The microphones were all placed at the same distance from the step forming an arc of constant radius. One of the microphones was oriented approximately normal to the top surface of the step. Surface pressure was also measured using flush mounted microphones. Six different step heights with three different flow speeds were examined. The far-field sound showed a clear dependence on step height with an increase of up to 3 dB between different heights. It was shown that the data scaled on $U^7$ and the sound was shown to have very little directionality.

Awasthi (2011) measured pressure fluctuations from flow over steps having heights significantly less than the incoming boundary layer thickness in an anechoic wind-tunnel. Pressure fluctuations at locations in the vicinity of the step and at large distances upstream and downstream of the step were recorded using flush mounted surface microphones. Three step heights were chosen with heights of 3.8%, 15%, and 60% of the boundary layer thickness. Two flow speeds of $U = 30$ m/s and $U = 60$ m/s were used for each of the three different heights. Results showed that disturbances caused by the step convect large distances downstream, and the pressure spectrum profile associated with the flow from the step was clearly distinguishable at as much as 152 step heights downstream. This effect was shown to be a strong function of step height.

Ji and Wang (2010) carried out an LES simulation of flow over backward and forward-facing steps using the incompressible Navier-Stokes equations in conjunction with the dynamic Smagorinsky model of Germano (1991) with Lilly's modification (Lilly 1992). The pressure Poisson equation was solved to determine the instantaneous pressure values in the vicinity of the step. The Reynolds number based on the step height and free-stream velocity ranged from 21,000 to 328 as the step height was varied from 53% to 0.83% of the unperturbed boundary layer thickness at the step. Results showed good agreement with Farabee and Casarella (1984, 1986). The far-field sound was calculated using Lighthill's theory with an approximate low-frequency Green's function for an acoustically compact step height. It was determined that the dominant acoustic source was a stream wise dipole normal to the face of the step. This observation was made under the assumption that sources on the top of the step would be negligible. They also report that the height of the step effects the sound radiation based on the acoustic source modification which is associated with the high vertical velocity up the face of the step.

Slomski (2011) performed LES calculations in order to separate the individual sources of sound in terms of the regions around the step. Sources of sound were separated into zones upstream and downstream of the step. The far-field contributions from the individual regions were compared to the total sound and the contribution from the step face alone was compared with the results of Ji and Wang (2010). The results were also compared with measurements taken in the Anechoic Flow Facility at the David Taylor Model

Basin. The results were in good agreement with the wind-tunnel measurements and also showed that the step face was not the sole contributor to the far-field sound as stated in Ji and Wang (2010). The conclusions stated that the area approximately $5h$ downstream of the step is the region generating the majority of the far-field sound.

Hao and Wang (2013) investigated the effect of sweep angle on the flow over a forward-facing step and the associated sound radiation using LES. Four sweep angles of $0°$, $15°$, $30°$, and $45°$ were examined. The step height remained constant at 13% of the unperturbed boundary layer. A major focus of this study was the "sweep-independence principle" which states that for an object presented to an incoming flow at some angle, the flow normal to the leading face of the object will be unaffected by the spanwise flow. It was shown that the reattachment lengths are almost completely insensitive to sweep angle. Velocity profiles normalized by the step-normal component of the free-stream velocity component collapsed well. The skin-friction coefficient defined in the direction normal to the step and normalized on the step-normal component of the free-stream velocity also collapsed well in the separation zones both upstream and downstream of the step. Taking the point of zero skin-friction downstream of the step to define the reattachment length it was shown that from $0°$ to $45°$ there was a reduction in separation length of only 9.7%. The mean wall pressure coefficient also showed good collapse when it was defined using the step-normal velocity component. These results support sweep independence. This study also examined the frequency spectra of the fluctuating surface pressure. It was shown that the lower frequency levels decreased with increasing sweep angle when normalized on the flow direction because of the decreasing step-normal velocity. The high frequency range is associated with small-scale turbulence and was largely unaffected by sweep angle. The spectra showed good agreement in low-frequency range when normalized on the step normal velocity but did not collapse at the higher frequencies. This finding speaks to the limitations of the sweep-independence principle. The sound pressure spectra was also calculated and showed good collapse in the low-frequency range and showed only minor deviation at higher frequencies for angles up to $30°$ when referenced on the step-normal component of the flow giving approximate validation of sweep-independence for the acoustic field. Finally, it was shown that the spanwise coherence of the source field increases significantly with increasing sweep angle which may have important implications for the current study.

Awasthi *et al* (2014) measured sound radiation from swept steps and from rounded swept steps in an anechoic wall jet facility. Angles from $0°$ to $30°$ were measured with rounding radii of 0%, 12.5%, 25%, and 50% of the step height. The ratio of step height to boundary layer thickness was 83% and the Reynolds number based on the step height was $Re_h = 1.62x10^4$. This work was also focused on validating the sweep independence principle for the acoustic field. The study also found that the sweep independence principle was approximately valid for angles up $30°$ when viewed from step-fixed observer locations. Again, it was shown that the sweep independence principle is most valid in the low-frequency range which is consistent with the findings of Hao and Wang (2013) despite the differences between the experimental and computational setup. The effect of the rounding behaved as it had in previous rounded step experiments reducing the sound level with each increase in radius.

Glegg (2012) developed a tailored Greens function for a step based on the Wiener-Hopf method. This Greens function is applied to a boundary layer flow over a backward and a forward-facing step using an approach developed by Doak. The results of the investigation state that the sound radiation is caused by a scattering mechanism which can be modeled using solutions for scattering on parallel semi-infinite plates given by Noble. It was shown that the far-field sound is characteristic of a streamwise dipole in the lowest frequency range and that the sound caused by turbulence in the area around the step scales on the sixth power of the mean velocity. The sound showed little directionality in the high frequency range. It was also noted that the effects of interference become important at high frequencies and there is a null a dip in the spectrum at certain angles. The results show good agreement with the wind tunnel measurements of Catlett (2010).

## B. Flow Around Cylinders

Sakamoto and Arie (1983) studied vortex shedding frequency from flow past a vertical rectangular prism and a vertical cylinder immersed in a turbulent boundary layer on a wall. Several different aspect ratios were examined in the context of the shedding frequency varying between 0.5 and 8 for the rectangular prism and between 1 and 8 for the circular cylinder. A separate set of aspect ratios ranging from 1 to 5 was used to measure the effect of the parameter $h/\delta$ on the Strouhal number. Hot-wire probes placed downstream were used to measure the vortex shedding and a smoke-wire was used for visualization. Reynolds numbers for this experiment ranged between $Re_\theta = 4128$ and 7332. Results show that a prominent shedding frequency is visible from prisms with aspect ratio above 1. For aspect ratios of 1 and lower no prominent frequency is found. This is supported by the results from examining the relationship between aspect ratio and Strouhal number which was shown to increase as aspect ratio increased. The same fundamental results were found for the circular cylinders. It was noted that in the graphs of aspect ratio versus Strouhal number, the lines change to a less steep slope at about $h/d = 2$ for the rectangular prisms and at about 2.5 for the circular cylinders.

Okamoto and Sunabashiri (1992) explored changes in vortex formation and the turbulent wake from cylinders of finite aspect ratio mounted to a plate in a wind-tunnel. Six aspect ratios of $H/D = 0.5, 1, 2, 4, 7,$ and 23.75 were used. The incoming boundary layer was approximately 4 mm giving a boundary layer-to-height ratio of $\delta/H = 0.11$. The Reynolds numbers ranged between $Re_D = 2.5\times10^4$ and $Re_D = 4.7\times10^4$. Surface pressure on the cylinders was recorded using a line of surface mounted sensors. The cylinders were rotated in order to record pressure over the entire circumference. The pressure coefficient in the wake of the cylinder varied along the length of the cylinder for cases with $H/D \leq 5$ because the free end effects reach to the base of the cylinder. In the case of $H/D = 1$ the effects of the free end could be seen along the entire length of the cylinder in the pressure measurements. In contrast, the case of $H/D = 7$ showed that the end effects were confined to the vicinity of the free end. This case showed two separate depressions in the surface pressure, while the case of $H/D = 1$ showed only one. This difference showed that the different cases exhibited different types of vortex shedding. Water channel ink shedding was used to visualize vortex activity around the cylinders. It was shown that the influence of the end effects on the vortices weakened with increasing aspect ratio and the relative size of the horseshoe vortices decreases. For the smaller aspect ratio cases it was shown that streamlines from the top of the cylinder reattach to the plate downstream forming a circulation zone behind the cylinder. In cases where end effects had influence along the entire length of the cylinder the circulation zone was shown to grow with increasing $H/D$, but the opposite was noted in the cases where the end effects were confined to the top of cylinder. Symmetric vortex shedding was seen in small aspect ratios and anti-symmetric vortex shedding was seen in the higher aspect ratios. The Strouhal number also decreased with increasing aspect ratio.

Fröhlich and Rodi (2004) presents LES data of flow around a surface-mounted cylinder of finite length. The cylinder had an aspect ratio of $H/D = 2.5$. The Reynolds number for the flow was $Re_D = 43000$ where $D$ is the diameter of the cylinder. The boundary layer thickness was 10% of the cylinder height. The study compared several simulations which used different numerical schemes and boundary conditions to ensure the independence of the results. The results indicated that the drag coefficient was decreased with decreasing height-to-diameter ratio due to the flow over the top of the cylinder interfering with the wake. It is also stated that drag increased with reduced boundary layer thickness $\delta/D$. Visualizations of the flow revealed that separation at the sharp front edge of the cylinder was regular, exhibiting lateral vortex rollers which intertwine and merge downstream. Flow around the downstream side of the cylinder's top edge showed a complex separation process which was attributed to the cylinders

curved trailing edge and the interaction from the side wall separation. Moving toward the base the flow became more regular. It was stated that symmetrical vortex shedding occurred near the bottom of the cylinder as a rare event. The irregular separation and shedding processes produced correspondingly irregular forces on the cylinder. It is also stated that the average flow exhibits an arch-type vortex behind the cylinder as with a wall-mounted cube and that further studies should examine the dependence of this feature on the height-to-diameter ratio.

## C. Bluff body Acoustics

In McEachern and Lauchle (1994) hydrophones were configured as cylinders in a cross flow in order to measure self-noise. The cylinders were towed through a quiet body of water at diameter based Reynolds numbers of between $Re_D = 4 \times 10^3$ and $1.8 \times 10^4$. Aspect ratios were examined in the range of 0.5 to 2.5 and the end cap geometry was also altered to give the sharp 90 degree edge a radius. The edge radii varied between $0.0315D$ to $0.5D$. This study considered an approximately laminar inflow in order to isolate the sources of turbulence created by the interaction of the body and flow. The results showed that in cylinders with aspect ratios below 1 the noise radiation from the cylinders decreased steadily with increasing Strouhal number and that the spectral level decreased with increasing end cap radius. The spherical end cap showed a decrease in the noise of 30 [dB]. In cylinders with aspect ratio greater than 1, the reduction in sound by the rounded end caps was still present but not nearly as strong and became negligible above $L/D = 2$. This supports the findings in Okamoto and Sunabashiri (1992) which stated that free end effects had little influence on pressure fluctuations for higher aspect ratios. It is stated that the rounded end caps prevented reattachment of the flow after separating at the front edge and that the reattachment of the flow was the major source of pressure fluctuations.

Watkins and Oswald (1999) studied the flow field and induced vibrations on externally mounted car mirrors in a wind-tunnel experiment. Hot-wire anemometers were used to measure mean velocities and turbulent intensities. Local velocities around the mirrors were seen to rise as much as 60% above the mean flow and as low as 40% below it. Local turbulent intensities were shown to be as high as 40%. Vibrations in the mirrors were measured both in the wind-tunnel and on the road showing frequencies above 20 Hz and good agreement for each case showing that the local aerodynamic sources were dominant over mechanical inputs such as road roughness or engine vibration. The study concludes that turbulent buffeting is the major source of this vibration as apposed to vortex shedding. While this study does not measure the far-field sound radiation the conclusions drawn about dominant aerodynamic sources are important to the subject.

Glegg *et al* (2014) outlines a model for separated flows over sharp corners having a separation bubble that periodically sheds vorticity. This theory was applied to the relatively simple case of a forward-facing step and achieved agreement with wind tunnel measurements presented in Catlett *et al* (2014).

The purpose of this paper is to develop a prediction method for the sound radiation from a cylindrical step or embossment mounted on a plate for which the cylinder's height is much smaller than its diameter as shown in Fig. 1. The results given above clearly indicate that the forward face of the embossment is the most likely source of sound, and this has been confirmed by the wind tunnel measurements shown below. To understand the detail of the cylinder flow we will first use RANS simulation to identify the separation region at the leading edge of the cylinder and to provide details of the mean flow. A noise prediction method will then be developed based on these observations and the theory given by Glegg *et al* (2104) for sound radiation from forward-facing steps. Finally the predicted spectra of the flow noise is compared against wind tunnel measurements.

## II.    Details of the Steady Flow

### A. Computational Methodology

A RANS simulation has been performed of the flow over the cylindrical embossment shown in Fig.1. The diameter of the cylinder is sufficiently large that it is greater than the acoustic wavelength at the frequencies of interest. When this configuration is examined experimentally the large diameter will allow for phased array measurements to target specific areas of the flow so that the characteristics at different points of interest can be identified. The aspect ratio of the cylinder is $h/2R=0.04$ and the computational domain used for the RANS calculations is $L_x$ x $L_y$ x $L_z= 6R$ x $0.35R$ x $5R$ or $120h$ x $70h$ x $100h$. The upstream inlet boundary conditions include a preformed logarithmic boundary layer profile, the side walls employ a slip condition, and the outlet is a Dirichlet pressure boundary. The top of the domain is a Dirichlet velocity boundary with a value equal to that of the mean flow in the streamwise direction and zero in all others. The k-omega SST turbulence model has been applied and was chosen for its ability to properly resolve boundary layer turbulence and to model separation. The flow parameters are presented in Table 1. The open source CFD software OpenFOAM was used with a steady-state solver for incompressible, turbulent flow.

### B. Separation at the Leading Edge

Fig. 2 shows a color plot of the mean pressure on the lower boundary and the top of the cylinder. The area in blue at the leading edge of the cylinder represents a low pressure zone caused by separation at the leading edge. In this area there is recirculation as there would be in a simple forward-facing step configuration, however the circulation area follows the curve of the cylinder across the leading edge. This curved circulation area creates a spiraling effect in the mean flow as shown in Fig 3. Each streamline spirals along the leading edge of the cylinder until it becomes aligned with the mean flow and is convected downstream.

Figure 4 shows contours of wall shear stress magnitude on the surfaces of the cylinder. An arc of low stress follows nearly the entire forward edge of the cylinder. Examining the $x$ and $z$ components of the shear stress we find that there is in fact reversed flow in this zone. Using the $x$ and $z$ components a vector of skin friction coefficient normal to the edge of the cylinder at several different angles is shown in Fig. 5. The portion of the graph in Fig. 4 which passes below zero represents the separation zone. When the line passes above zero, the flow has reattached. The results show that the reattachment length is nearly constant up to approximately 50 degrees. After 50 degrees the reattachment length increases as shown in Fig. 6.

The simulation revealed some interesting characteristics of the flow. The separation zone at the leading edge resembles that of a forward-facing step except that it is curved along the leading edge. This similarity suggests that the noise should also be similar to a forward-facing step. The prediction scheme presented below is dependent on this similarity and so its use is supported by the results of the simulation.

If the leading edge is similar to a forward-facing step then it should follow that the trailing edge is similar to a backward-facing step. It has been shown in previous studies that the sound from backward-facing steps is negligible compared with that from forward-facing steps. The RANS simulation showed that there are some interesting interactions between streamlines released from the circulation zone and the wake, but the experimental results, which will be presented latter, suggest that these interactions do not influence the sound radiation.

**Table 1**

| Parameter | Value |
|---|---|
| $U_\infty$ | 60 [m/s] |
| $Re_\theta$ | 51226 |
| $Re_x$ | 3826530 |
| $\delta$ | 0.098 [m] |
| $h/\delta$ | 0.255 |
| $\nu$ | 1.586e-5 [m²/s] |

# III.  Far Field Sound Level Predictions

## A. The Sound Field from Flow Over a Step

The sound prediction from a surface can be calculated using Lighthill's acoustic analogy and Curle's theorem. The acoustic field is given by:

$$\rho'(\mathbf{x},t)c_\infty^2 = \int\limits_{-T}^{T}\int\limits_{S} p_{ij}(\mathbf{y},\tau)n_j\frac{\partial}{\partial y_i}G(\mathbf{x},t\,|\,\mathbf{y},\tau)dS(\mathbf{y})d\tau + \int\limits_{-T}^{T}\int\limits_{V} T_{ij}(\mathbf{y},\tau)\frac{\partial^2}{\partial y_i\partial y_j}G(\mathbf{x},t\,|\,\mathbf{y},\tau)dV(\mathbf{y})d\tau \qquad (1)$$

where $\rho'$ is the density perturbation, $c_\infty$ is the speed of sound, $p_{ij}$ is the compressive stress tensor that includes both unsteady pressure and shear stresses applied to the surface, $G$ is a suitable Green's function which is a solution to the wave equation, and $T_{ij}$ is Lighthill's stress tensor. Taking the Fourier transform with respect to time and considering the fluctuating viscous shear stress on the surface to be negligible, the acoustic pressure becomes

$$p(\mathbf{x},\omega) = -\int\limits_{S} p(\mathbf{y},\omega)\frac{\partial G_\omega(\mathbf{x}\,|\,\mathbf{y})}{\partial n}dS(\mathbf{y}) + \int\limits_{V} T_{ij}(\mathbf{y},\omega)\frac{\partial^2 G_\omega(\mathbf{x}\,|\,\mathbf{y})}{\partial y_i y_j}dS(\mathbf{y}) \qquad (2)$$

The volume source terms in Eq.(2) are quadrupoles and therefore their magnitude will be of order of the Mach number $M$ less than the surface terms which are of dipole order, and so, for low Mach number flows the volume integral may be dropped.

## B. Green's Function for a Step

For flow noise sources near a flat rigid surface, defined by the plane $y_2 = 0$ (Neumann Boundary conditions), the Green's function is conveniently defined by the radiated field from a point source and its image source of equal positive strength below the boundary as:

$$G_\omega(\mathbf{x} \mid \mathbf{y}) = \frac{e^{ik|\mathbf{x}-\mathbf{y}|}}{4\pi|\mathbf{x}-\mathbf{y}|} + \frac{e^{ik|\mathbf{x}-\mathbf{y}^*|}}{4\pi|\mathbf{x}-\mathbf{y}^*|} \tag{3}$$

where $\mathbf{x}$ is the observer location, $\mathbf{y}$ is the source location, and

$$|\mathbf{x}-\mathbf{y}| = r = \sqrt{(x_1-y_1)^2 + (x_2-y_2)^2 + (x_3-y_3)^2} \qquad |\mathbf{x}-\mathbf{y}^*| = r^* = \sqrt{(x_1-y_1)^2 + (x_2+y_2)^2 + (x_3-y_3)^2}$$

For a 2-dimensional step with the observer located at $x_3 = 0$ the derivatives of the Green's function are

$$\frac{\partial G_\omega(\mathbf{x} \mid \mathbf{y})}{\partial y_1} = -\frac{ikx_1}{r_o}\left(\frac{e^{ikr_o}}{2\pi r_o}\right)\cos\left(\frac{kx_2 y_2}{r_o}\right)$$

$$\frac{\partial G_\omega(\mathbf{x} \mid \mathbf{y})}{\partial y_2} = -\frac{kx_2}{r_o}\left(\frac{e^{ikr_o}}{2\pi r_o}\right)\sin\left(\frac{kx_2 y_2}{r_o}\right) \tag{4}$$

When Eq. (4) is used in Eq. (2) and the pressure fluctuations on faces of the step are acoustically compact we obtain

$$p_s(\mathbf{x},\omega) = \frac{ke^{ikr_o}}{2\pi r_o} \int_{-\infty}^{\infty}\left(\frac{ix_1}{r_o}\cos\left(\frac{khx_2}{r_o}\right)F_1(\mathbf{y},\omega) + \frac{x_2}{r_o}\sin\left(\frac{khx_2}{r_o}\right)F_2(\mathbf{y},\omega)\right)dy_3 \tag{5}$$

where $F_1$ and $F_2$ are the forces per unit span on the face and top of the step respectively. If the step is also acoustically compact in the spanwise direction then phase variation becomes negligible and we can move the propagation terms outside of the integral and, assuming the force on the face and top of the step to be equal (Glegg *et al* (2014)), we have

$$p_s(\mathbf{x},\omega) = \frac{k}{2\pi r_o}\left(\frac{ix_1}{r_o}\cos\left(\frac{khx_2}{r_o}\right) + \frac{x_2}{r_o}\sin\left(\frac{khx_2}{r_o}\right)\right)\int_{-\infty}^{\infty}\left[F(\mathbf{y},\omega)\right]dy_3 \tag{6}$$

Finally taking the spectrum of Eq. (6) gives

$$S_{pp}(\mathbf{x},\omega) = \frac{k^2 S_{FF}(\omega)}{(2\pi r_o)^2}\left|\frac{ix_1}{r_o}\cos\left(\frac{khx_2}{r_o}\right) + \frac{x_2}{r_o}\sin\left(\frac{khx_2}{r_o}\right)\right|^2 \tag{7}$$

where $S_{FF}(\omega)$ is the spectrum of the forcing on the faces of the step.

## C. The Forcing Spectrum

The study by Glegg *et al* (2014) obtained an empirical fit to the far field data of sound radiation from a step based on the results obtained by Catlett *et al* (2014). For a straight step it was found that

$$G_{pp}(\mathbf{x},f) = \frac{(kh)^2 \, Ll \, K_s (\rho_o U^2)^2 h}{(2\pi r_o)^2 \, U(1+(\omega h/U)^2)^{7/3}} \left| \frac{ix_1}{r_o} \cos\left(\frac{khx_2}{r_o}\right) + \frac{x_2}{r_o}\sin\left(\frac{khx_2}{r_o}\right) \right|^2$$

where                                                                                 (8)

$$1K_s = 3.61 \times 10^{-7} \text{ m}$$

and $G_{pp}(\mathbf{x},f)$ is the one sided spectral density of the far field pressure at the observer in units of Pa$^2$/Hz, $r_o$ is the distance from the step to the observer (m), $L$ is the length of the step (m), $U$ is the flow speed normal to the step (m/s), $K_s$ is a nondimensional constant and $l$ is the spanwise correlation length scale (m). Figure 7 shows a comparison of this formula to the spectra measured by Catlett et al (2014). Although this formula has provided some good agreement to measured spectra, the high frequencies are under predicted and the factor $K_s$ is adjusted to achieve the best fit to the data which creates some uncertainty. The directionality term assumes that force from the top of step is equal to the force on the face.

A recent investigation has shown that a mixed scaling in which the level scales on step height $h$ and the frequencies scale on boundary layer thickness $\delta$ is more accurate and is given by

$$G_{pp}(\mathbf{x},f) = \frac{(k\delta)^2 \, Ll \, K_s (\rho_o U^2)^2 h}{(2\pi r_o)^2 \, U(1+(\omega\delta/U)^2)^{7/3}} \left| \frac{ix_1}{r_o} \cos\left(\frac{khx_2}{r_o}\right) + \frac{x_2}{r_o}\sin\left(\frac{khx_2}{r_o}\right) \right|^2 \qquad (9)$$

The prediction formula given in Eq. (8) was compared with spectral data from Catelett et al (2014) and also with data from Ji and Wang (2010) and it was found that a frequency scaling, which is only dependent on $h$ in Eq.(8), does not properly account for the effect of incoming turbulence on the peak frequencies. This was resolved by scaling the frequencies on the boundary layer thickness $\delta$, which was constant in each study, as shown in Eq.(9). It was also found that the slope of the spectral shape was not constant between different experiments and may be dependent on other parameters of the flow, although the exact nature of this dependence is still not clear. As the slope of the spectrum was adjusted it was also found that the value of $1K_s$ needed to be adjusted as well. For the most consistent predictions, this value fell within a range of $10^{-3} < 1K_s < 10^{-2}$. It was also found that an improved prediction could be obtained if the force on the front face of the step was not restricted to being equal to the force on the top of the step. A modified form of the prediction formula is then

$$G_{pp}(\mathbf{x},f) = \frac{(k\delta)^2 \, Ll \, K_s (\rho_o U^2)^2 h}{(2\pi r_o)^2 \, U(1+(\omega\delta/U)^2)^{7/3}} \left| \frac{ix_1}{r_o} \cos\left(\frac{khx_2}{r_o}\right) + Q\frac{x_2}{r_o}\sin\left(\frac{khx_2}{r_o}\right) \right|^2 \qquad (10)$$

which includes a factor $Q$ in the directionality term which corresponds to the ratio of force on the top face of the step to the force on the front of the step. For observer angles near 90° there is under prediction of the dip in the spectra in the high frequency range using Eq. (9). The inclusion of the factor $Q$ improves the prediction of the high-frequency directionality. However, for predictions at observer angles significantly greater or less than 90° this term is detrimental and distorts the effects of the directionality. Figure 8 shows a prediction with $Q = 0.5$ and $1K_s = 4 \times 10^{-2}$.

## D. Application to a 3D Cylinder

If the step is three dimensional the surface integral needs to be carried out in more detail. For a cylindrical step, as shown in Fig. 1, with its axis aligned with the $y_2$ direction, and $y_1 = R\cos\theta$, $y_3 = R\sin\theta$, the normal directions along the sides of the cylinder will be a function of $\theta$. The acoustic field can then be specified as the sum of two surface integrals, the first defined by $S_f$ is on the side of the cylinder and the second, $S_T$, includes the top of the cylinder $y_2 = h$ and the plate surface where $y_2 = 0$ . This gives

$$p(\mathbf{x},\omega) = -\int_{S_f} p(\mathbf{y},\omega)\left\{\frac{\partial G_\omega(\mathbf{x}|\mathbf{y})}{\partial y_1}n_1 + \frac{\partial G_\omega(\mathbf{x}|\mathbf{y})}{\partial y_3}n_3\right\}dS - \int_{S_T} p(\mathbf{y},\omega)\frac{\partial G_\omega(\mathbf{x}|\mathbf{y})}{\partial y_2}n_2 dS$$

$$n_i = \left(\cos(\theta),1,\sin(\theta)\right)$$

(11)

By choosing the Greens function defined above the integral over the surface where $y_2 = 0$ is eliminated because $\partial G/\partial y_2 = 0$ on $y_2 = 0$.

Then, in cylindrical coordinates, we have:

$$p_s(\mathbf{x},\omega) = -\int_0^{2\pi}\int_0^h p(\mathbf{y},\omega)\left[\frac{\partial G_\omega(\mathbf{x}|\mathbf{y})}{\partial y_1}\cos\theta + \frac{\partial G_\omega(\mathbf{x}|\mathbf{y})}{\partial y_3}\sin\theta\right]_{R=a} dy_2 a\,d\theta$$

$$-\int_0^{2\pi}\int_0^a \left[p(\mathbf{y},\omega)\frac{\partial G_\omega(\mathbf{x}|\mathbf{y})}{\partial y_2}\right]_{y_2=h} R\,dR\,d\theta$$

(12)

where $a$ is the radius of the cylinder and $R$ is the radial coordinate. The first integral is evaluated along $R = a$, and the second integral is evaluated on $y_2 = h$.

## E. Summing of Individual Sources

To simplify the analysis we will assume that the pressure fluctuations are concentrated around the outer rim and vertical face of the cylinder, and are only locally correlated. This implies that we can treat the integral about the circumference as the sum of a set of $N$ locally correlated sources, and write

$$p_s(\mathbf{x},\omega) = -\sum_{n=1}^N \int_{\theta_n-\Delta\theta/2}^{\theta_n+\Delta\theta/2}\int_0^h \left[p(\mathbf{y},\omega)\left\{\frac{\partial G_\omega(\mathbf{x}|\mathbf{y})}{\partial y_1}\cos\theta + \frac{\partial G_\omega(\mathbf{x}|\mathbf{y})}{\partial y_3}\sin\theta\right\}\right]_{R=a} dy_2 a\,d\theta$$

$$-\sum_{n=1}^N \int_{\theta_n-\Delta\theta/2}^{\theta_n+\Delta\theta/2}\int_0^a \left[p(\mathbf{y},\omega)\frac{\partial G_\omega(\mathbf{x}|\mathbf{y})}{\partial y_2}\right]_{y_2=h} R\,dR\,d\theta$$

(13)

where $\theta_n = n\Delta\theta$ and $\Delta\theta = 2\pi/N$ and we will choose $N$ to match the correlation length scale of the problem. The advantage of taking this approach is that we can now apply the far-field approximation to the Greens function for each segment of the surface. The far-field approximation gives the propagation distance from each segment as

$$r = r_n - \frac{(x_1 - a\cos\theta_n)(y_1 - a\cos\theta_n)}{r_n} - \frac{x_2 y_2}{r_n} - \frac{(x_3 - a\sin\theta_n)(y_3 - a\sin\theta_n)}{r_n}$$

$$r_n = ((x_1 - a\cos\theta_n)^2 + x_2^2 + (x_3 - a\sin\theta_n)^2)^{1/2}$$

and similarly for the image sources with $y_2$ replaced by $-y_2$. This allows the Greens functions to be defined as

$$\frac{\partial G_\omega}{\partial y_1} = \left( \frac{ik(a\cos\theta_n - x_1)e^{ikr_n}}{2\pi r_n^2} \right) \cos\left( \frac{ky_2 x_2}{r_n} \right) e^{-ik(y_1 - a\cos\theta_n)(x_1 - a\cos\theta_n)/r_n - ik(y_3 - a\sin\theta_n)(x_3 - a\sin\theta_n)/r_n}$$

$$\frac{\partial G_\omega}{\partial y_2} = -\left( \frac{kx_2 e^{ikr_n}}{2\pi r_n^2} \right) \sin\left( \frac{ky_2 x_2}{r_n} \right) e^{-ik(y_1 - a\cos\theta_n)(x_1 - a\cos\theta_n)/r_n - ik(y_3 - a\sin\theta_n)(x_3 - a\sin\theta_n)/r_n} \quad (14)$$

$$\frac{\partial G_\omega}{\partial y_3} = \left( \frac{ik(a\sin\theta_n - x_3)e^{ikr_n}}{2\pi r_n^2} \right) \cos\left( \frac{ky_2 x_2}{r_n} \right) e^{-ik(y_1 - a\cos\theta_n)(x_1 - a\cos\theta_n)/r_n - ik(y_3 - a\sin\theta_n)(x_3 - a\sin\theta_n)/r_n}$$

## F. The Acoustically Compact Segment

We next make the assumption that the segments are acoustically compact so that we may ignore any phase variation over each segment when evaluating the surface integrals. This allows us to take the Greens functions outside of the surface integrals so

$$p_s(\mathbf{x}, \omega) = -\sum_{n=1}^{N} \left[ \frac{\partial G_\omega(\mathbf{x}|\mathbf{y})}{\partial y_1} \cos\theta_n + \frac{\partial G_\omega(\mathbf{x}|\mathbf{y})}{\partial y_3} \sin\theta_n \right]_{\substack{R=a \\ \theta=\theta_n \\ y_2=h}} \times \int_{\theta_n - \Delta\theta/2}^{\theta_n + \Delta\theta/2} \int_0^h \left[ p(\mathbf{y}, \omega) \right]_{R=a} dy_2 a\, d\theta$$

$$- \sum_{n=1}^{N} \left[ \frac{\partial G_\omega(\mathbf{x}|\mathbf{y})}{\partial y_2} \right]_{\substack{R=a \\ \theta=\theta_n \\ y_2=h}} \times \int_{\theta_n - \Delta\theta/2}^{\theta_n + \Delta\theta/2} \int_0^a \left[ p(\mathbf{y}, \omega) \right]_{y_2=h} R\, dR\, d\theta \quad (15)$$

## G. The Source Terms

In previous work (Glegg *et al* (2014)) it is assumed that the force per unit span on the front face of the step is equal to the force per unit span on the top face of the step. Consequently we can define the force per unit span on each segment of the cylinder as

$$F(\theta, \omega) = \int_0^h \left[ p(\mathbf{y}, \omega) \right]_{R=a} dy_2 = \int_0^a \left[ p(\mathbf{y}, \omega) \right]_{y_2=h} \left( \frac{R}{a} \right) dR \quad (16)$$

where the first integral refers to the step face and the second to the top surface of the step. Using this to replace the integrals in Eq.(10) gives the far field pressure as

$$p_s(\mathbf{x},\omega) =$$

$$-\left\{\sum_{n=1}^{N}\lim_{y\to h}\left[\frac{\partial G_\omega(\mathbf{x}\,|\,\mathbf{y})}{\partial y_1}\cos\theta_n + \frac{\partial G_\omega(\mathbf{x}\,|\,\mathbf{y})}{\partial y_3}\sin\theta_n\right]_{\substack{\theta=\theta_n\\R=a}} + \sum_{n=1}^{N}\lim_{R\to a}\left[\frac{\partial G_\omega(\mathbf{x}\,|\,\mathbf{y})}{\partial y_2}\right]_{\substack{\theta=\theta_n\\y_2=h}}\right\} \times \int_{\theta_n-\Delta\theta/2}^{\theta_n+\Delta\theta/2}F(\theta,\omega)a\,d\theta \qquad (17)$$

### H. The Far-field Spectral Density

The next step is to define the power spectrum of the acoustic field defined as

$$S_{pp}(\mathbf{x},\omega) = \frac{\pi}{T}Ex\left[|\,p_s(\mathbf{x},\omega)|^2\right] \qquad (18)$$

This will depend on

$$S_{FF}(\theta,\omega) = \frac{\pi}{T}\int_{\theta_n-\Delta\theta/2}^{\theta_n+\Delta\theta/2}\int_{\theta_m-\Delta\theta/2}^{\theta_m+\Delta\theta/2}Ex[F(\theta,\omega)F^*(\theta',\omega)]a^2\,d\theta\,d\theta'$$

which is the double integral of the cross spectrum of the force per unit span. Note that we have allowed for the range of the integration to be different for $\theta$ and $\theta'$. However if we take the increment in angle to be large enough that the spanwise range of the integration exceeds the correlation length scale, then we can model this function as

$$S_{FF}(\theta_n,\omega) = S_{ff}(\theta_n,\omega)l\,a\Delta\theta\delta_{nm} \qquad (19)$$

where $S_{ff}(\omega,\theta_n)$ is the spectrum of the unsteady force per unit span at the angle $\theta_n$ and $\ell$ is the spanwise correlation length scale. We then obtain

$$S_{pp}(\mathbf{x},\omega) = \sum_{n=1}^{N}\frac{k^2 S_{ff}(\theta_n,\omega)l\,a}{(2\pi r_n)^2}|\beta_n|^2\Delta\theta$$

$$\beta_n = \left(\frac{a-x_1\cos\theta_n - x_3\sin\theta_n}{r_n}\right)\cos\left(\frac{khx_2}{r_n}\right) - i\left(\frac{x_2}{r_n}\right)\sin\left(\frac{khx_2}{r_n}\right) \qquad (20)$$

It should be noted that the directionality term $\beta_n$ suggests that the face and top of the step are correlated and in phase which may not necessarily be correct since the two forces may be uncorrelated. However this is inconsequential as the two forces are in quadrature and so the same result would be the same if the two forces are completely uncorrelated.

### I. Prediction Formula

Applying the empirical fit for the forward-facing step, given by Eq. (9), to the theory developed for the cylinder gives the far-field sound as

$$G_{pp}\left(\mathbf{x},f\right)=\sum_{n=1}^{N}\frac{(k\delta)^2 1 K_s a(\rho_o U_n^2)^2 h}{\left(2\pi r_n\right)^2 U_n (1+(\omega\delta / U_n)^2)^{7/3}}\left|\beta_n\right|^2\Delta\theta$$

(21)

where $U_n$ is the mean flow speed that applies at each location along the step. It has been shown by Hao and Wang (2013) that this velocity should be chosen as the flow velocity normal to the step face, and so in principle $U_n=U_s\cos\theta_n$ where $U_s$ is the flow speed of the approaching flow.

# IV.     Results and Discussion

## A. Experimental Arrangement

### 1.  Virginia Tech Stability Wind Tunnel

The measurements of far field sound from cylindrical embossment were performed in Virginia Tech Stability Wind Tunnel which is a closed return subsonic facility capable of providing large Reynolds number flow conditions. The facility is capable of reaching Reynolds number of 5 Million with very low free stream turbulence levels (0.031% at 57m/s). The facility is unique in that it can operate in both aerodynamic and anechoic configuration due to two separate 7.3m x 1.83m x 1.83m test sections that can be switched between the two configurations. In its full anechoic configuration the side walls of the test section are formed by tensioned Kevlar which is acoustically transparent but contains the flow. The floor and ceiling of the test section are also made up of Kevlar through the use of several panels. The test section is sandwiched between two anechoic chambers that are lined with acoustic grade foam wedges to minimize the reflections from the test section allowing far field sound measurements to be made with high signal to noise ratio (SNR). Figure 9 (a) shows the anechoic test section during a typical airfoil trailing edge noise measurement. More details on this anechoic configuration of Virginia Tech Stability Wind Tunnel can be found in Devenport *et al* (2013). Recently this anechoic configuration has been modified to perform boundary layer noise measurements by replacing the starboard side Kevlar window with a hard surface (false wall) on which the boundary layer can be grown. This semi-anechoic false wall configuration has been shown in Fig. 9 (b). The flow enters the test section after passing a 5.5m x 5.5m settling chamber with seven turbulence reducing screens and a 9:1 area ratio contraction. The contraction wall is faired with the false wall using a smooth transition fairing as shown in Fig. 9 (b). The incoming boundary layer is tripped using a 9.5mm trip installed on the contraction fairing which is also shown in Fig. 9 (b). The false wall is adjustable in the wall-normal direction so that a zero pressure gradient boundary layer can be obtained after which surface geometry to be tested is installed on this wall. More details on the false wall configuration of Virginia Tech Stability Wind Tunnel can be found in Awasthi *et al.* (2014). The undisturbed boundary layer thickness for 9.5mm trip used in present work were measured by Awasthi et al. (2014) and are approximately 97mm and 95mm for free stream velocities of 30m/s and 60m/s respectively.

### 2.  Cylindrical Embossment

The circular cylinder geometry used in the present work was installed on the false wall 4.35m downstream of the boundary layer trip. The height of the cylinder is 25.4mm which is approximately 25% of the undisturbed boundary layer thickness. The diameter of the embossment is 914.4mm which provides an aspect ratio of $h/D$=0.027. The cylinder is installed so that its spanwise centerline lies approximately 933.5mm above the floor of the test section which is about 18.5mm above the spanwise center of the test section. Figure 10 shows the cylinder mounted on the false wall of the facility. The Reynolds numbers based on the cylinder height at which measurements were made range from 31,600 to 94,900 which correspond to free stream velocities between 20m/s and 60m/s. The range of Reynolds number range based on the cylinder diameter is 1,137,600 to 3,416,400.

### 3. Far Field Sound Instrumentation

The measurements of far field sound from the cylinder were made using a 117 microphone phased array. The frontal face of this phased array has been shown in Fig. 11(a). For the present measurements the phased array was installed in the port side anechoic chamber with its frontal face 805 mm from the Kevlar window as shown in Fig. 11(b). The face of the array is kept parallel to the flow. The array was positioned such that its center was approximately 60.3mm below that spanwise center of the disk. The streamwise location of the center of the array was 231mm upstream of the leading edge of the disk.

The phased array consists of Panasonic WM-64PNT electret microphones arranged in a spiral fashion on a circular carbon-fiber disk (Fig. 11(a)). These microphones have a flat frequency response between 20 Hz and 16 kHz with a sensitivity of $-44 \pm 3$ dB Re 1V/Pa at 1 kHz. The microphones were calibrated and were selected to be within $\pm 5^o$phase and $\pm 0.4$ dB amplitude between 500 Hz and 16 kHz. Boundary layer refraction effects, convective effects, pressure doubling due to the microphones being mounted on a solid surface, and attenuation through the Kevlar cloth are all accounted for in post-processing. Data from the microphones are recorded simultaneously at 51200Hz for 32 seconds with two 64 channel PCI-based data acquisition cards. The cards have a total of 11 normally unused channels of which 6 were used to record simultaneous signals from six of the near-field array mics. Signals are processed through an anti-aliasing filter at 20 kHz. Spectral quantities are computed by averaging the Fourier transform of blocks of 8192 samples. The diagonal of the cross-spectrum is removed in order to omit uncorrelated noise in the beamformed maps. All the beamformed maps discussed in present work are referenced to the center of the array which as pointed out earlier is slightly upstream of the embossment. Figure 12 shows the observer location in relation to the embossment i.e. the location of the array center with respect to the embossment.

## B. Acoustic Measurements

The beamformed maps are further cleaned by rejecting background noise from the facility using a de-convolution procedure. The background rejected maps are finally integrated to within region of interest to yield the sound spectrum. Figure 13(a) shows an example of a beamformed sound source map at 2 kHz frequency and free stream velocity of 60m/s. Also shown on the figure are the location of the embossment on the false wall and the region outside which the sound sources were rejected. The background rejected sound source map is shown in Fig. 13(b) along with the location of the embossment. It can be seen that the de-convolution procedure clearly removes the extraneous sound sources due to the facility and reveals the sound from the embossment which is centered mostly around the leading edge of the geometry. Similar maps exist at different frequencies and though they are not shown here they also show the leading edge of the embossment to be the dominant sound source. This leading edge region is also the region with flow separation indicated by the RANS simulation.

Maps similar to the one shown in Fig. 13(b) are integrated to yield the frequency spectrum of the far field sound. The integration region picked for the present work has also been shown in Fig. 13(b). It should be noted that the integration of the beamformed maps is only performed where the sound from the embossment is clearly visible. Figure 13 also shows that the area identified by the phased array measurements is in agreement with the separation area given by the RANS simulation. The simulation shows that the separation zone occupies the majority of the leading edge and this is consistent with the size of the source given by the phased array data.

Figure 14 shows the integrated sound spectrum for the embossment at 4 different free stream velocities of 30, 40, 50 and 60m/s. Note that the spectra are shown only for a frequency range between 800Hz and 10 kHz due to low SNR outside this range. Additionally only those data points within this frequency range are shown for which the beamformed show a clear presence of sound source from the embossment. The spectra are consistent through the low frequency range and begin to decay slowly into the high-frequency range where the directionality of the sound causes a trough in the sound levels at approximately 7 kHz. For each increment of 10 m/s in flow speed the sound level increases by approximately 6 dB. Figure 15 shows the spectra from the cylinder normalized on the flow speed and the height of the step as suggested by Catlett *et al* (2014). The spectra do not collapse consistently on this scaling and there is a 2 dB increment between each flow speed, which will be discussed in more detail below.

### C. Comparison of Predictions with Measurements

The prediction given by Eq. (21) has been applied to spectra presented in Fig. 16 with $|K_s = 9 \times 10^{-1}$. In Fig. 17, the exponent of the spectral shape given in Eq. (21) has been changed from 7/3 to 5/3 and $|K_s = 5 \times 10^{-2}$. The results show that the 5/3 slope gives a better match to the slope of the spectra. This may be the consequence of the different wind tunnels used for the measurements because the 7/3 slope was based on Catlett's (2014) measurements that were made in a different wind tunnel.

The prediction shows good agreement in the low-frequency range, especially for higher freestream velocities. The slope of the spectral shape decreases as the velocity decreases and the prediction deviates from the measured spectra by up to 3 dB at the lowest speed. This is thought to be caused by a Reynolds number effect. In the high-frequency range the directionality of the sound becomes apparent and causes the dip at 7 kHz that is consistent at all flow speeds. However, the dip in the directionality is more pronounced than the measurements suggest. If the $Q$ factor described in section III part C is set to 0.25, the predictions are greatly improved as shown in Fig. 18. This gives a better fit to the high-frequency range for all the velocities. With this additional factor the low-frequency prediction becomes slightly less accurate.

## V.    Conclusions

The sound prediction scheme presented in Glegg *et al* (2014) has been applied to a cylindrical embossment. RANS simulation has shown that the leading edge of the cylinder has a separation zone similar to that of a forward-facing step. With this similarity and the application of the sweep independence principle, a prediction method for the sound radiation from flow over a cylindrical embossment has been developed. The approach is to separate the edge of the cylinder into elements which behave as forward-facing steps with an angle of incidence relative to the flow. The sum of the sources over the surfaces of the cylinder then give the total sound field. The application of an empirical fit to the sound spectra for flow over a forward-facing step gives the spectral shape and scaling of the sound from the cylinder.

Phased array measurements taken in an anechoic wind tunnel have shown that the leading edge separation zone is the dominant source of sound throughout the frequency spectrum. The phased array data has been integrated to give the spectrum of the sound which has a spectral shape similar to that of an axial dipole aligned with the flow. Spectral data for a cylinder which is has an aspect ratio of 1/36 was recorded at four different flow speeds of 30, 40, 50, and 60 m/s. Predictions compared with the spectra show good agreement in the low-frequency range, but under predict the dip in the spectra at 7 kHz. Reducing the relative magnitude of the force on the top surface of the cylinder improves the predictions giving a better fit to the dip in the high-frequency range.

## Acknowledgments

## References

Awasthi M., Forest J. B., Morton M. A., Devenport W., Glegg S., 2011, "The Disturbance of a High Reynolds Number Turbulent Boundary Layer by Small Forward Steps", 17th AIAA/CEAS Aeroacoustics Conference, June 6th-8th, Portland OR, AIAA-2011-2777.

Awasthi, M., Devenport, William J., Glegg, Stewart A. L. and Forest, Jonathan B., 2014, "Pressure fluctuations produced by forward steps immersed in a turbulent boundary layer", Journal of Fluid Mechanics, vol. 756, pp. 384-421.

Awasthi M., Devenport W., Meyers T., Alexander N., Glegg S., 2014 "Aeroacoustics of 2D and 3D Surface Discontinuities" 20th AIAA/CEAS Aeroacoustics Conference, Atlanta GA, June 2014

Catlett, M.R., 2010, "Flow Induced Noise from Turbulent Flow over Steps and Gaps", Master's Thesis, AOE Department, Virginia Tech. Avail: http://scholar.lib.vt.edu/theses/available/etd-05172010-192806/unrestricted/Catlett_MR_T_2010.pdf

Catlett, M.R., Devenport, W., Glegg S., 2014, "Sound from Boundary Later Flow over Steps and Gaps", Journal of Sound and Vibration 333 (2014), pp. 4170-4186

Devenport, William J., Burdisso R.A., Borgoltz A., Ravetta P.A. and Barone M.F, 2013, "The Kevlar-Walled Anechoic Wind Tunnel", Journal of Sound and Vibration, vol. 332, pp. 3971-3991.

Farabee, T. M., and Casarella, M. J., "Measurements of Fluctuating Wall Pressure for Separated/Reattached Boundary Layer Flows." ASME Journal of Vibration, Acoustics, Stress, and Reliability in Design, Vol. 108, 1986, pp. 301-307.

Farabee, T. M., and Zoccola, P. J., "Experimental Evaluation of Noise due to Flow over Surface Steps", 1998 ASME International Mechanical Engineering Congress and Exposition.

Glegg, S., "The Tailored Green's Function for a Forward Facing Step", Journal of Sound and Vibration (2012), http://dx.doi.org/10.1016/j.jsv.2012.09.037

Glegg, S., Bryan B., Devenport, W., Awasthi, M., 2014, "The Noise from Separated Flows", 20th AIAA/CEAS Aeroacoustics Conference, Atlanta GA, June 2014

Hao, J., Wang M., 2013, "Flow Noise from Swept Steps in Turbulent Boundary Layers", 19th AIAA/CEAS
Aeroacoustics Conference, Berlin, Germany, May 2013

Ji, M. and Wang M., 2010, "Sound Generation by Turbulent Boundary Layer Flow over Small Steps", Journal of Fluid Mechanics, vol. 654, pp. 161-193.

Okamoto, Shiki, and Yukisada Sunabashiri. "Vortex Shedding From a Circular Cylinder of Finite Length Placed on a Ground Plane." *Journal of Fluids Engineering* 114.4 (1992): 512. Web.

Mceachern, James F. "Flow-induced Noise on a Bluff Body." *The Journal of the Acoustical Society of America* 97.2 (1995): 947. Web.

Sakamoto, Hiroshi, and Mikio Arie. "Vortex Shedding from a Rectangular Prism and a Circular Cylinder Placed Vertically in a Turbulent Boundary Layer." *Journal of Fluid Mechanics* 126.-1 (1983): 147. Web.

Slomski, J. F., 2011, "Numerical Investigation of Sound from Turbulent Flow over a Forward Facing Step", 17th AIAA/CEAS Aeroacoustics Conference, Portland OR, June 2011

Watkins, Simon, and Greg Oswald. "The Flow Field of Automobile Add-ons — with Particular Reference to the Vibration of External Mirrors." *Journal of Wind Engineering and Industrial Aerodynamics* 83.1-3 (1999): 541-54. Web.
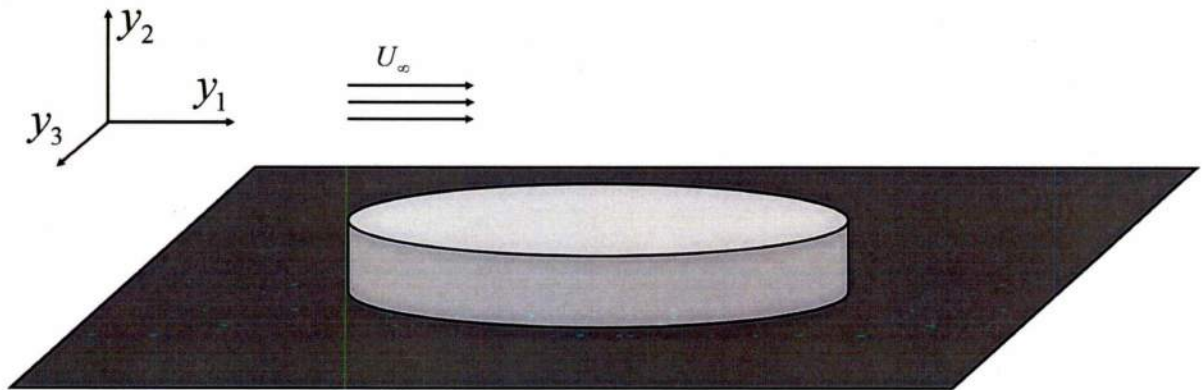
**Figure 1.** Cylindrical embossment on a flat plat with flow in the $y_1$ direction.
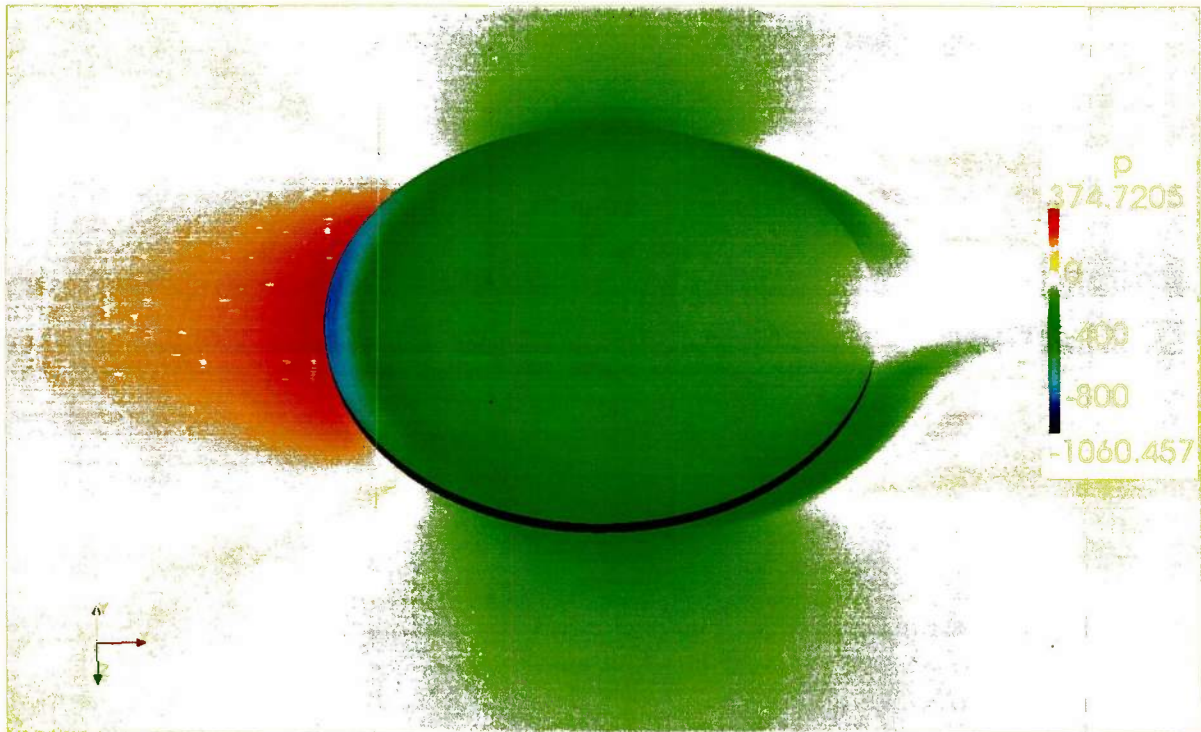


**Figure 2.** Contours of pressure on the lower boundary and the top of the cylinder given in Pascals divided by the density [m²/s²]. The blue area represents the recirculation area.
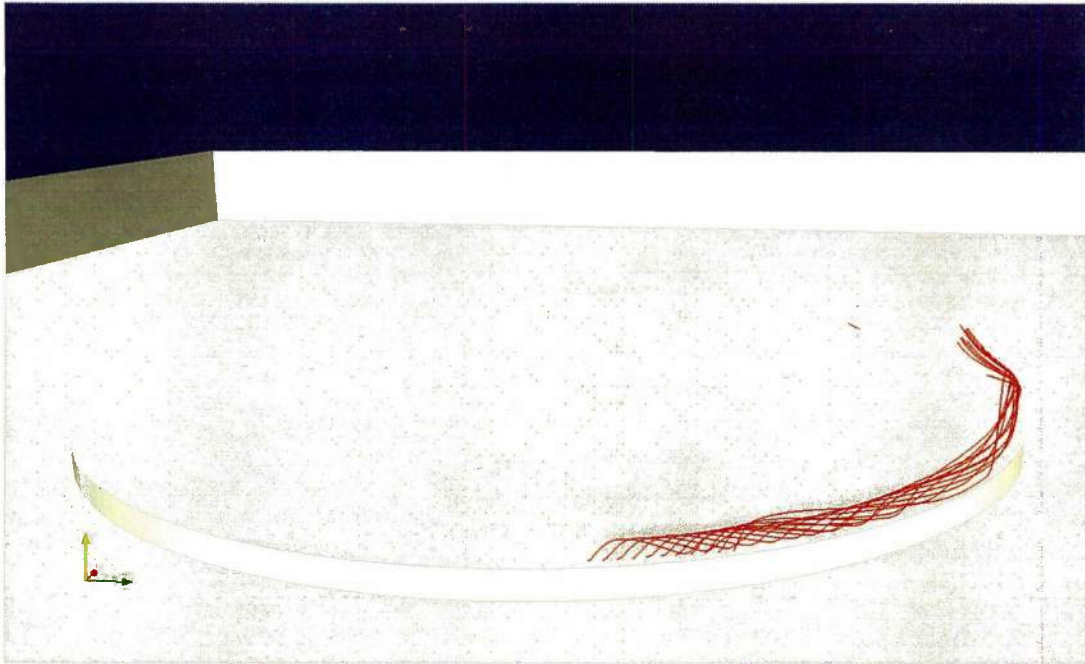
**Figure 3.** Streamlines released from a line inside the circulation area viewed from upstream of the cylinder
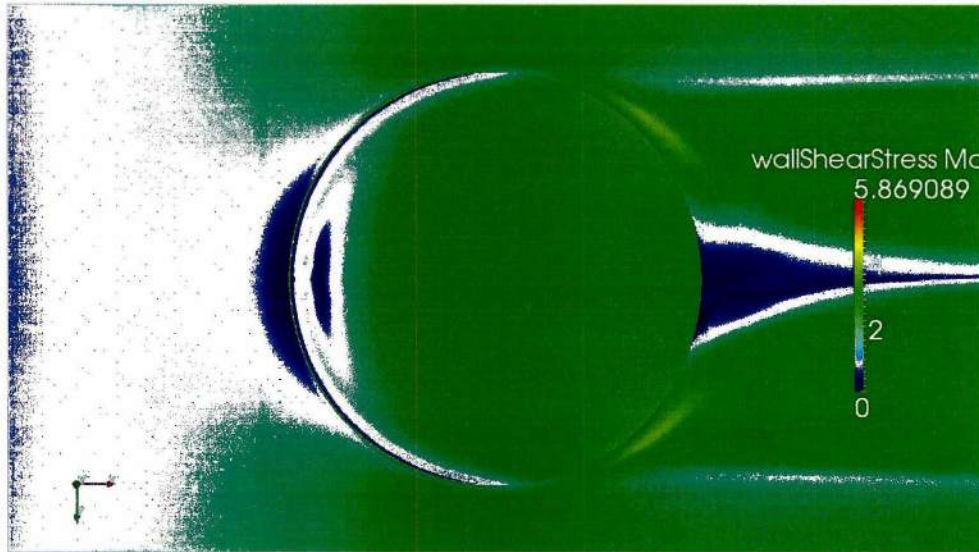


**Figure 4.** Contours of wall shear stress magnitude in Pascals divided by the density $[m^2/s^2]$ on the lower boundary and the top of the cylinder.
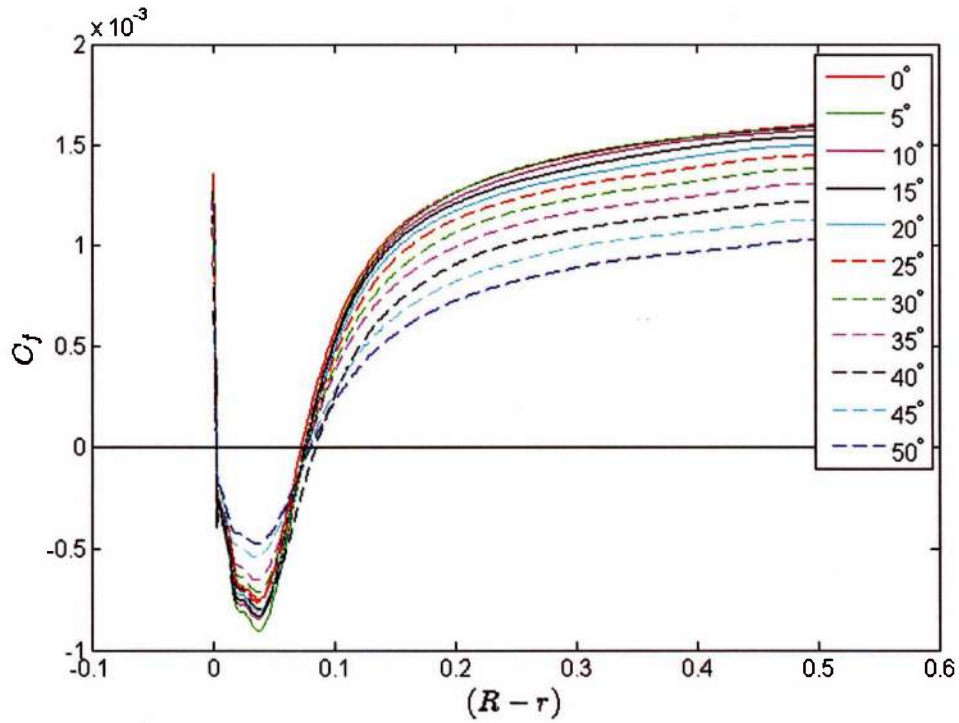
**Figure 5.** Coefficient of friction normal to the cylinder's leading edge.
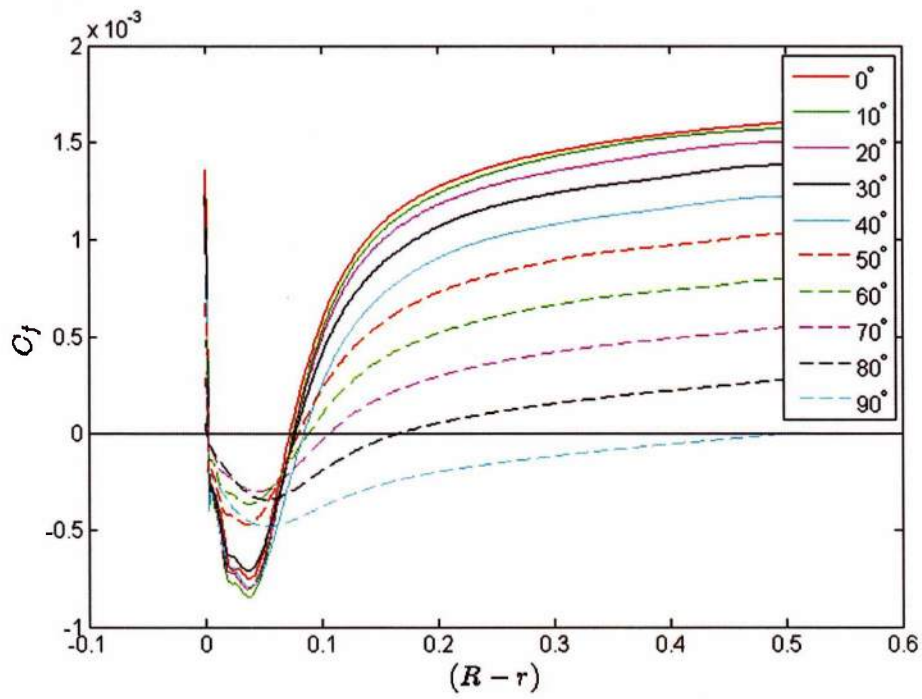


**Figure 6.** Coefficient of friction normal to the cylinder's leading edge at larger angles.
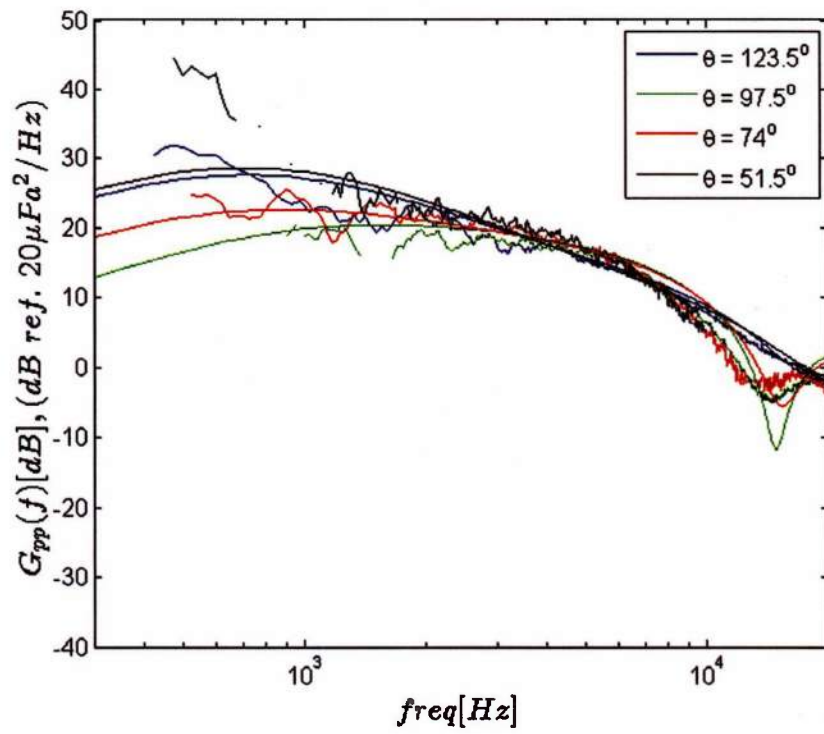
**Figure 7.** The fit of the empirical formula given by Eq. (8) to Catlett' *et al* (2014) data.
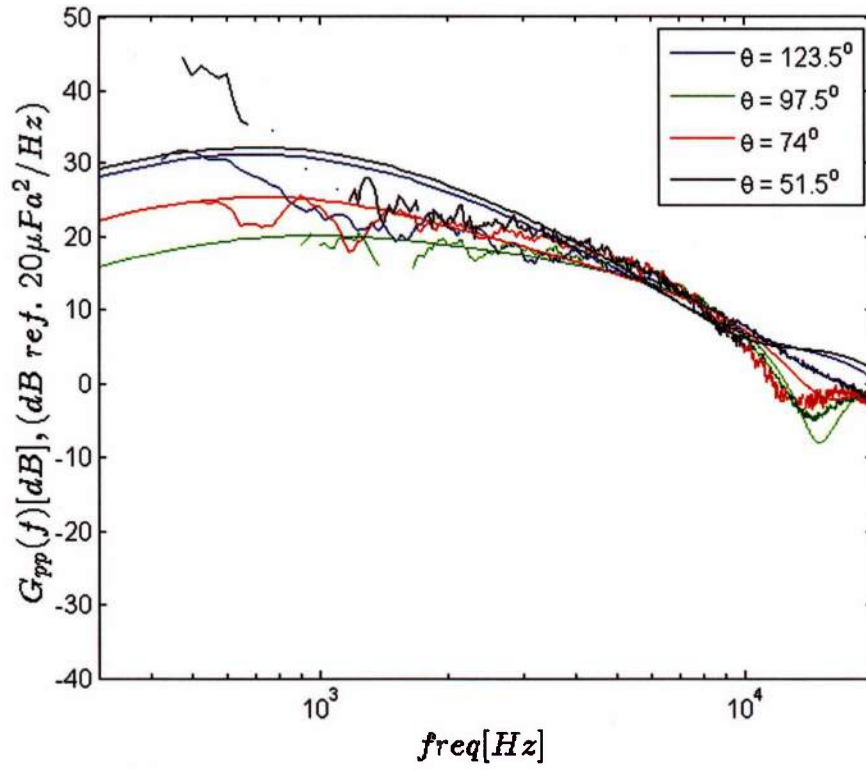
**Figure 8.** Prediction given by Eq. (8) including $Q$.
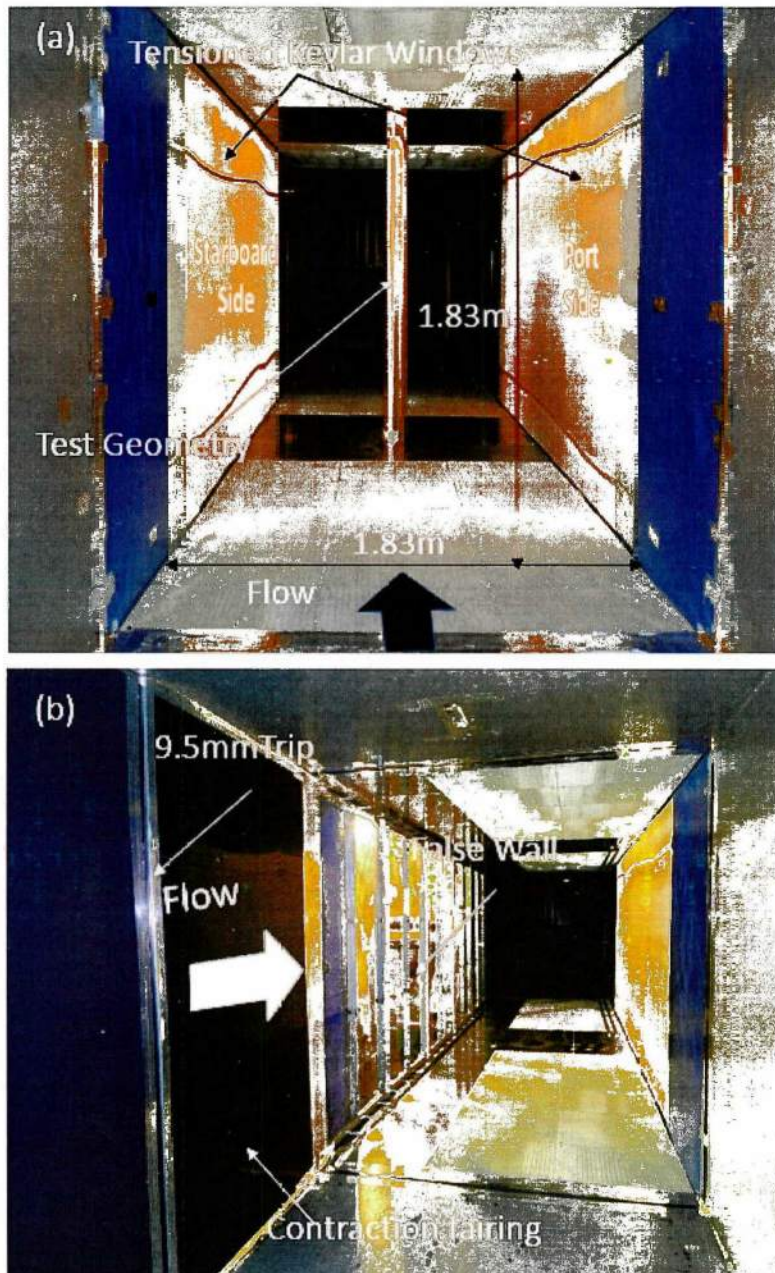
**Figure 9.** Anechoic test section of Virginia Tech Stability Wind Tunnel. (a) Full anechoic configuration, (b) Semi anechoic false wall configuration for boundary layer noise measurements.
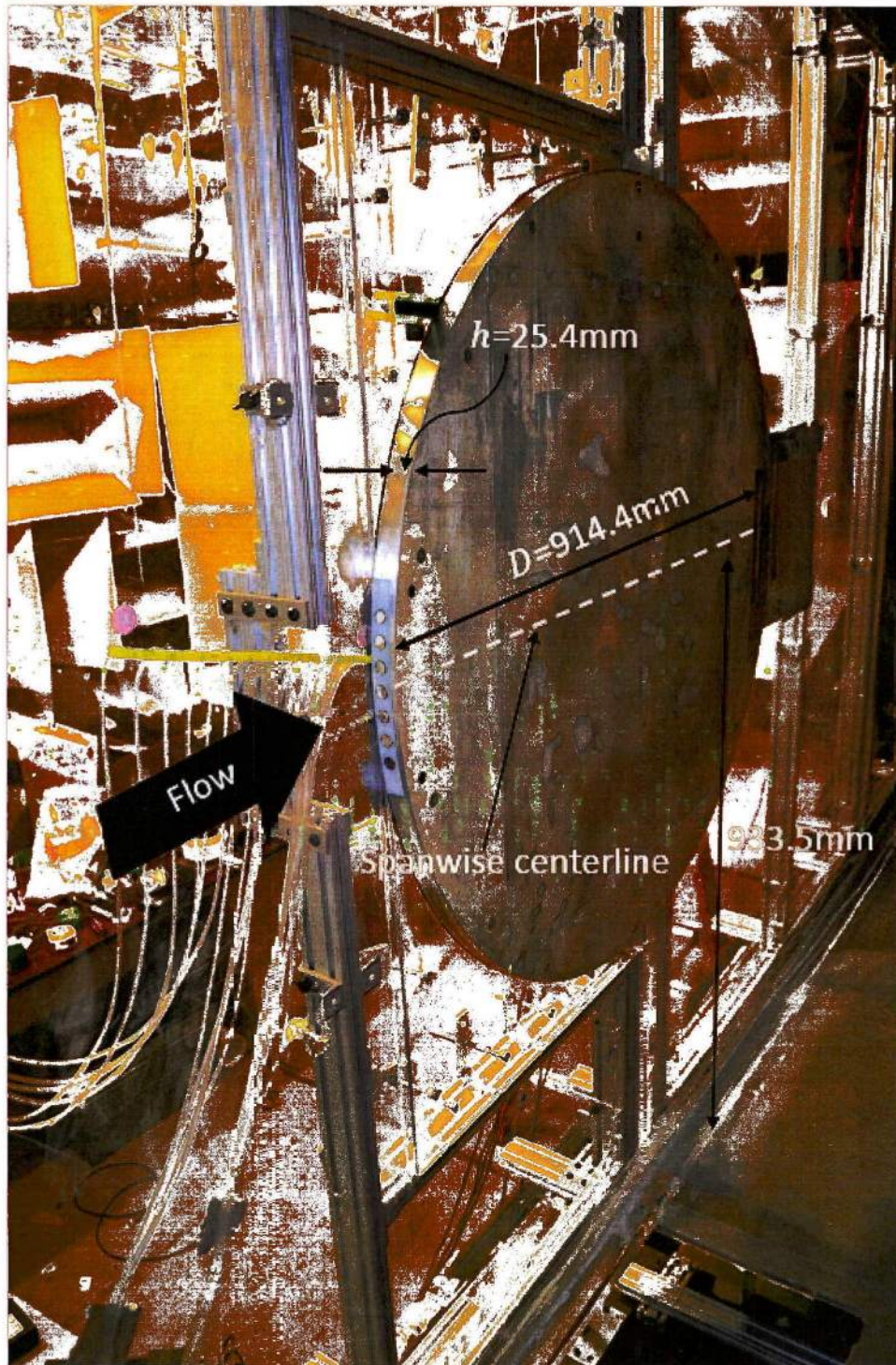
**Figure 10.** Cylindrical embossment installed on the false wall of Virginia Tech Stability Wind Tunnel.
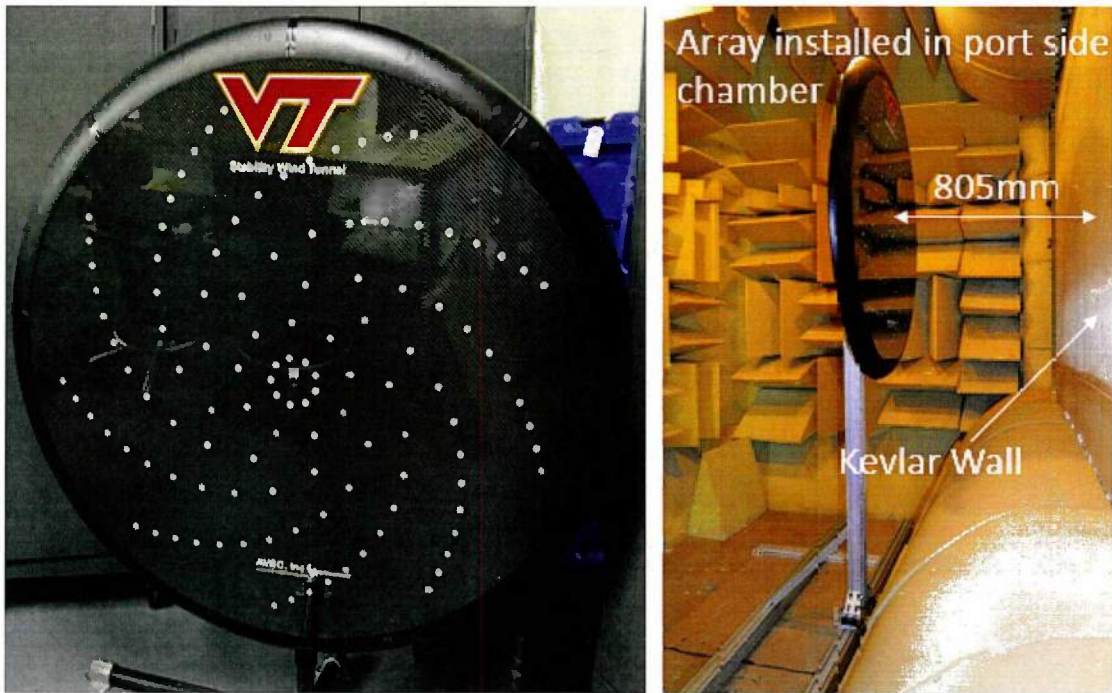
Figure 11.    Phased array for far field sound measurement. (a) Frontal face showing all 117 microphones arranged in spiral arms, (b) Phased array installed in the port side anechoic chamber directly facing the false wall (not shown) on the starboard side.
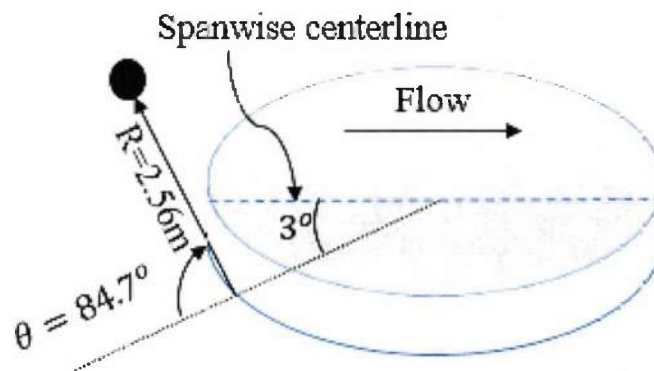


Figure 12.    Observer location corresponding to the center of the phased array for in relation to the position of cylindrical embossment on the false wall.
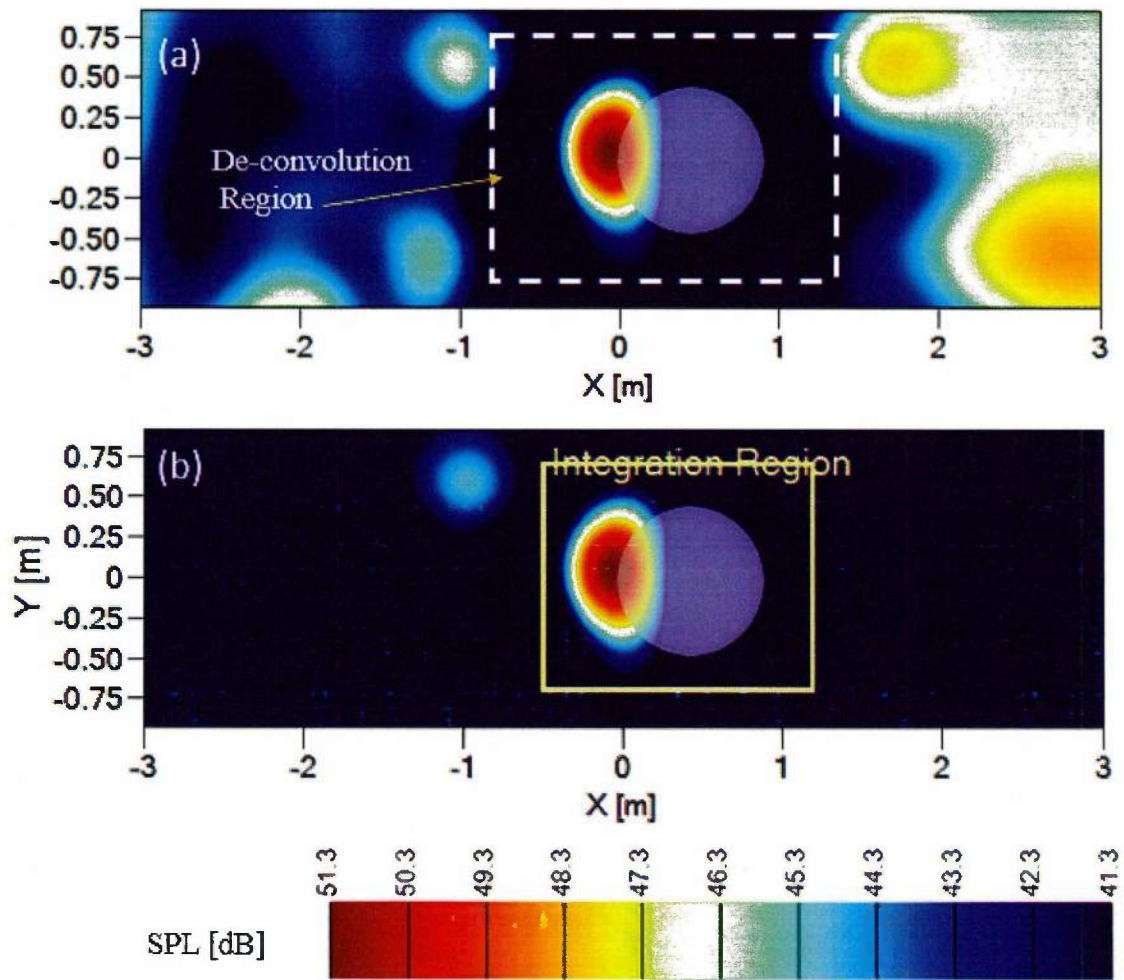
Figure 13.        Sound source maps at f=2 kHz and $U_\infty$=60m/s for cylindrical embossment. (a) Beamformed map, (b) Post de-convolution background rejected sound source map with integration region shown. Also shown on each figure is the location of cylindrical embossment on the wall. The contour scale (in dB) has been shown at the bottom of the figure.
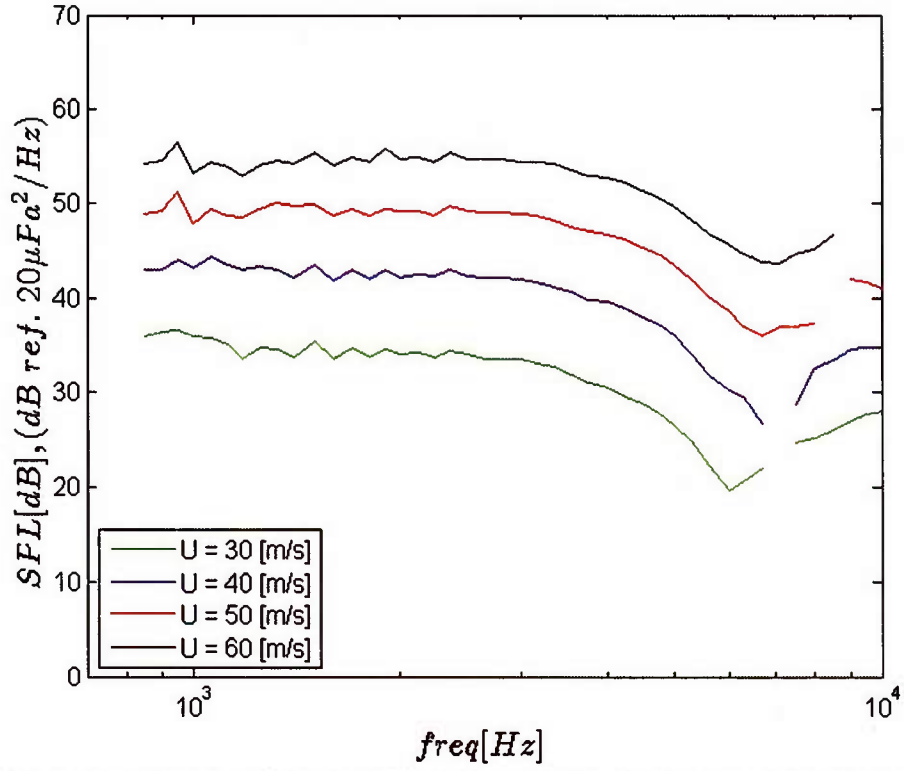
**Figure 14.** Spectra of sound from integrated phased array measurements for four different flow speeds at an angle of 84° above the streamwise center line of the cylinder.
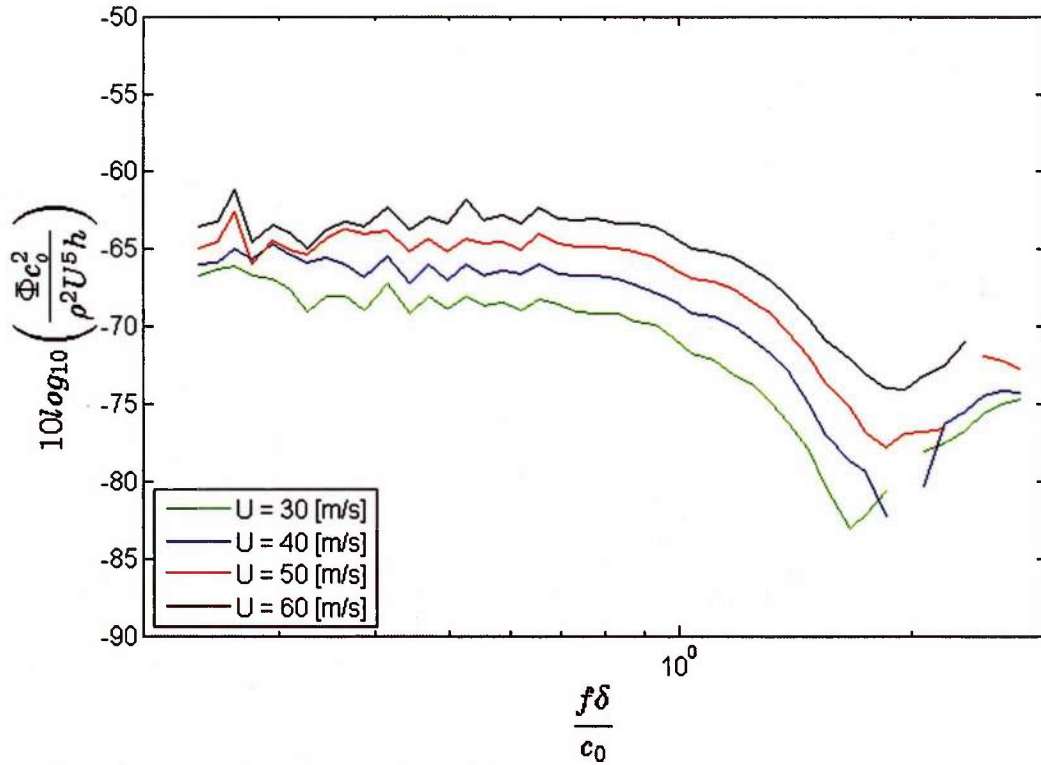
**Figure 15.**        Spectra from the cylinder with levels normalized on flow speed and step height and frequency normalized on boundary layer thickness.
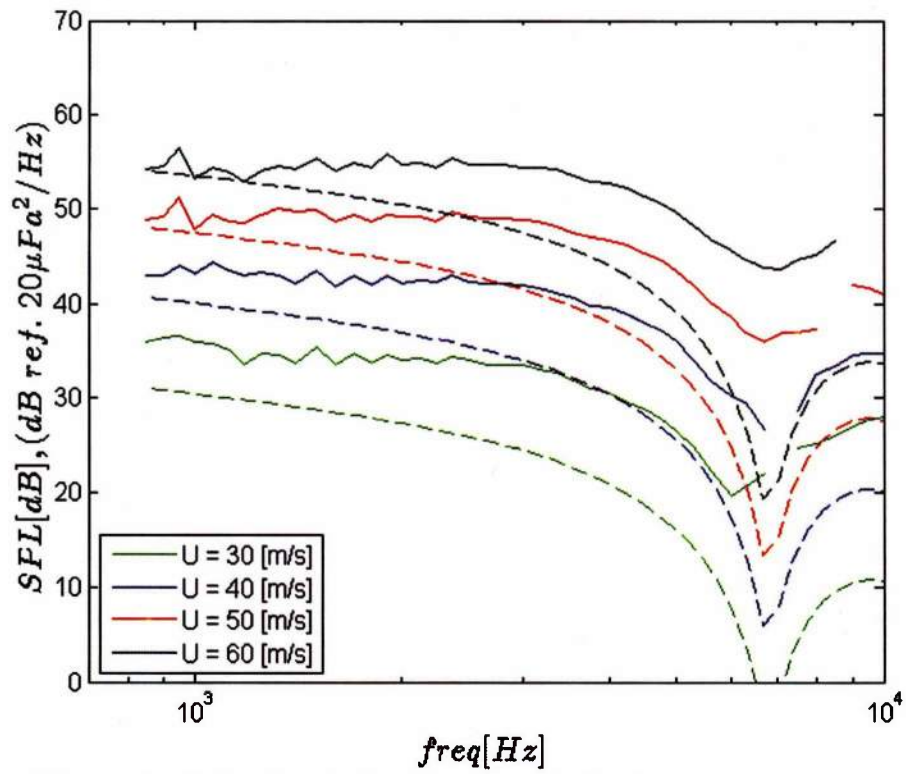
**Figure 16.**     Prediction given by Eq. (21) compared with measured spectra (Predictions are dashed lines).
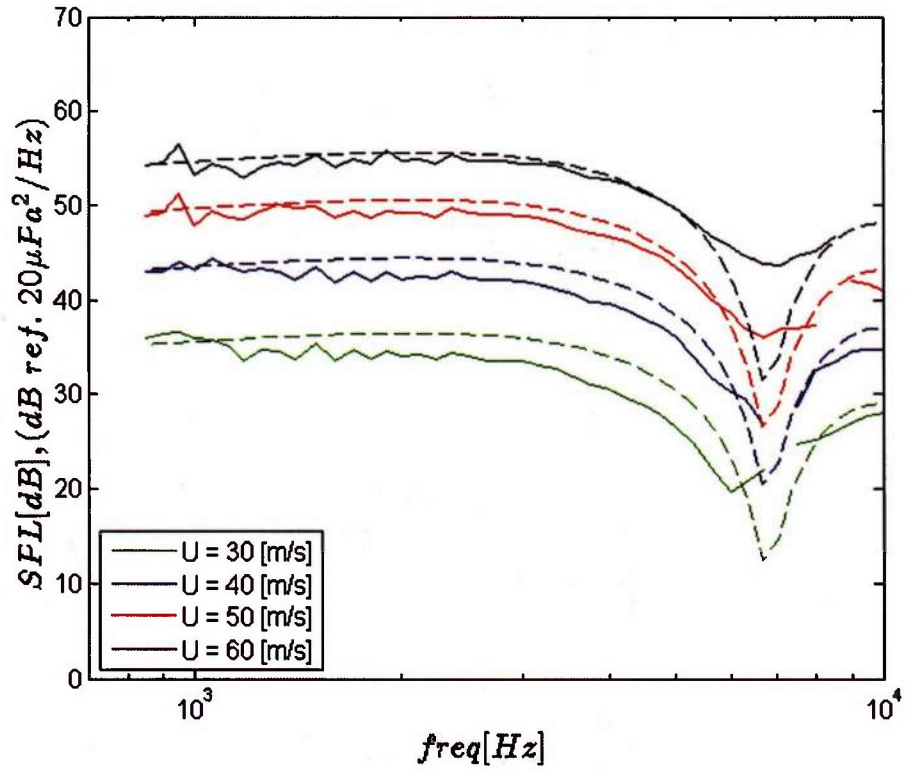
**Figure 17.** Prediction given by Eq. (21) with spectral shape exponent of 5/3 compared with measured spectra.
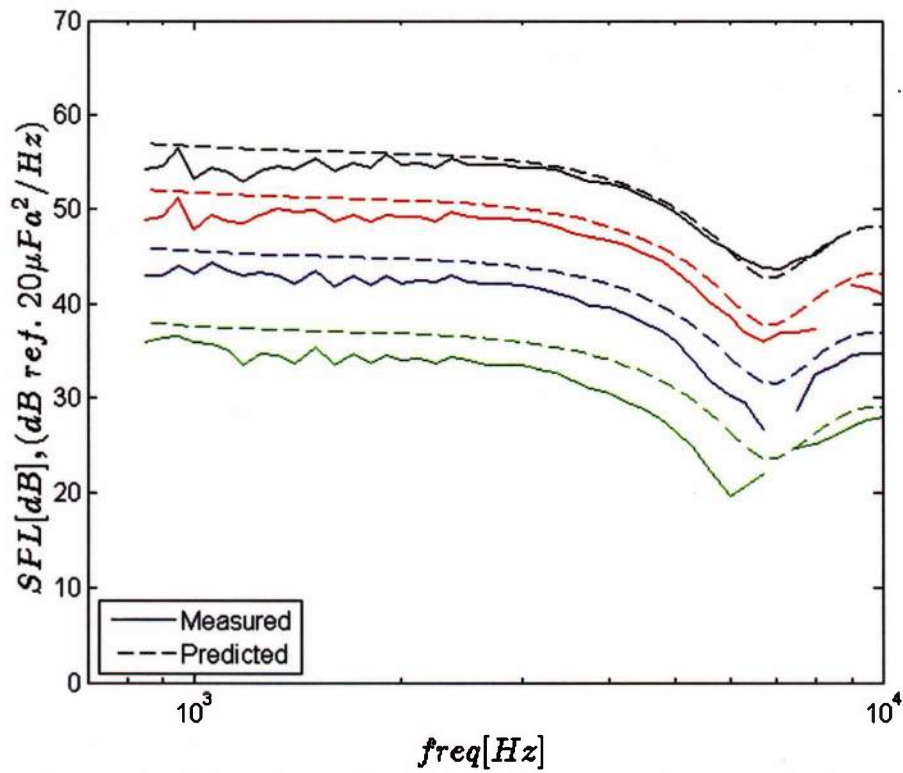
**Figure 18.** Prediction given by Eq. (21) including the directional damping factor $Q$ compared with measured spectra.